CHALMERS

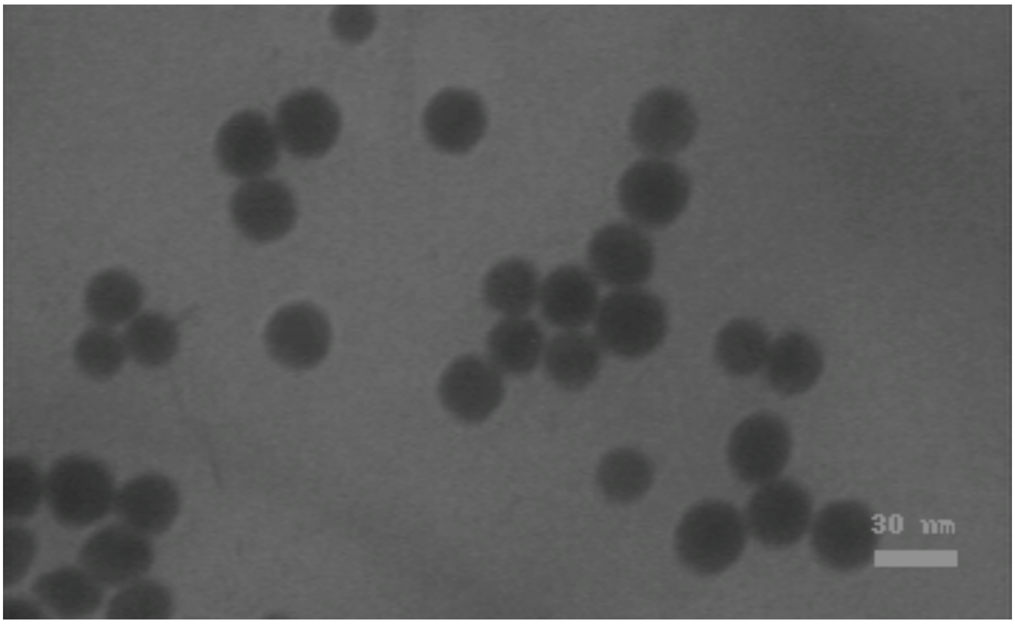

Gold Nanoinclusions in Thermoelectric Germanium Clathrates

Master of Science Thesis

PHAM HOANG NGAN

Department of Chemical and Biological Engineering
Division of Applied Surface Chemistry
CHALMERS UNIVERSITY OF TECHNOLOGY
Göteborg, Sweden, 2011

THESIS FOR THE DEGREE OF MASTER OF SCIENCE

Gold Nanoinclusions in Thermoelectric Germanium Clathrates

PHAM HOANG NGAN

CHALMERS

Supervised by Richard Ralph Heijl

Examined by Professor Anders Palmqvist

Applied Surface Chemistry
Department of Chemical and Biological Engineering
CHALMERS UNIVERSITY OF TECHNOLOGY
Göteborg, Sweden 2011

This thesis was carried out in the framework of the
Erasmus Mundus Master program of Nanoscience and
Nanotechnology
with the trajectory
Katholieke Universiteit Leuven (Belgium) –
Chalmers University of Technology (Sweden)
2009-2011

Gold Nanoinclusions in Thermoelectric Germanium Clathrates

PHAM HOANG NGAN

Applied Surface Chemistry,
Department of Chemical and Biological Engineering
Chalmers University of Technology
SE-412 96 Göteborg
Sweden
Telephone + 46 (0)31-772 1000

Local Promoter:
Professor Anders Palmqvist, Chalmers University of Technology

Supervisor:
Ph.D. student Richard Ralph Heijl, Chalmers University of Technology

Co-Promoter:
Professor Steven De Feyter, Katholieke Universitiet Leuven

Cover:
Transmission electron microscopy image of gold nanoparticles in solution C.
Göteborg, Sweden 2011

ABSTRACT

The focus of this master thesis project was to synthesize thermoelectric germanium clathrates with gold nanoinclusions of different particle sizes and study the influence of gold nanoparticle size on thermal conductivity of obtained clathrates. For this purpose, gold nanoparticle solutions of different particle sizes and with narrow size distributions were first prepared by a seeding and growth method. Then, they were subjected to purification and drying processes. Second, germanium clathrate $Ba_8Ga_{16}Ge_{30}$ was synthesized by solid state reaction between Ba, Ga and Ge elements at elevated temperature. Third, the prepared gold nanoparticles were introduced into synthesized clathrate by mixing them together and processing them to tablet samples using spark plasma sintering. Finally, tablet samples were subjected to thermal conductivity measurement. The results show a clear effect when gold nanoparticles were introduced into $Ba_8Ga_{16}Ge_{30}$ and an influence of gold nanoparticle sizes on thermal conductivity of obtained samples.

ACKNOWLEDGEMENTS

I would like to thank my promoter, Professor Anders Palmqvist for giving me the opportunity to work on this exciting and interdisciplinary project and guiding me dedicatedly throughout my work. I also would like to thank my supervisor Richard Ralph Heijl who was always with me, helped me during the time I did my thesis. I feel grateful for their kind support and continuous encouragement.

I would like to thank to other members of the Department of Chemical and Biological Engineering for contributing their valuable experience and time to solve practical as well as theoretical problems I encountered during my work.

I gratefully acknowledge the Erasmus Mundus Master of Nanoscience and Nanotechnology Program that bring me this great scholarship to study in prestigious Katholieke Universiteit Leuven and Chalmers University of Technology. The study is a milestone in my life.

And, deeply thank to my family for giving me everlasting and strongest motivation and bringing me to this stage of my life. I also would like to send my special thank to my close friends who always back me and help me to overcome sadness I had when being far away from home.

CONTENTS

Chapter 1

Introduction

As is becoming increasingly accepted, energy supply is a challenge to meet for sustainable development. Conventional fossil fuel is a limited resource and nuclear power is still facing serious safety issues. Renewable energy such as solar, wind, hydroelectric and biomass energy is expected to become increasingly important as future energy sources. Thermoelectric energy conversion has the potential to become an important technology for more efficient use of energy. Thermoelectric devices can operate over a wide range of temperature and be used as advanced coolers, for power generation by waste heat harvesting from household, industrial and aerospace applications. Besides working independently as the source of energy, thermoelectric devices have a special credible application in enhancing the efficiency of combustion engines. This is based on the awareness that the energy lost in contemporary combustion engine is around 60%.

The thermoelectric effects include the conversion of thermal to electrical energy (Seebeck effect) and vice versa (Peltier effect). These two phenomena were discovered by Thomas Johann Seebeck (1821) and Jean Charles Athanase Peltier (1834). The relationship between Seebeck and Peltier effects was found by William Thomson. He reported that it is possible to produce reversible heating or cooling in a material due to the flowing of electrical current through two joined dissimilar conductors. More recently, there has been much effort spent on applications of thermoelectric energy and searching for highly efficient thermoelectric materials.

The purpose of this work is to explore the advantages of introducing metallic nanoinclusions into bulk polycrystalline thermoelectric material. Nanostructures of polycrystalline materials add contributions of phonon scattering at interfaces. Energy barriers at interfaces may scatter phonons that carry heat more efficiently than the scattering of electrons that carry electrical current. Introduction of nanoparticles thus on the one hand contributes to the scattering of phonons, on the other hand creates a potential that may filter low energy electrons. The generated potential is expected to affect high energy electrons to a lower degree. By that, a decrease in thermal conductivity may be achieved with negligible change in electrical conductivity. Also, the increase in the fraction of high energy electrons could result in the enhancement of the Seebeck coefficient. As a total effect, the thermoelectric properties of bulk polycrystalline thermoelectric material with metallic nanoinclusions are expected to be improved. This study includes measurement of thermal conductivity of the sintered tablets. However, also measurements of electrical conductivity and Seebeck coefficient will be performed on the prepared materials at a later stage.

Chapter 2

Theory

2.1. Thermoelectric effect

The thermoelectric effect in general consists of three effects: the Seebeck and Peltier phenomena, and the Thomson relation.

The Seebeck phenomenon is the generation of a voltage potential when there is a thermal gradient applied on a material. When one end of a thermoelectric bulk is heated, carriers are thermally stimulated. Carriers with high thermal energy (in hot ends) tend to diffuse to regions of carriers with low thermal energy (cold ends), which results in a voltage difference between the two ends of the material (Figure 1a). The ratio of the voltage potential generated and the applied thermal difference is defined as the Seebeck coefficient: [1]

$$S = \frac{\Delta V}{\Delta T}$$

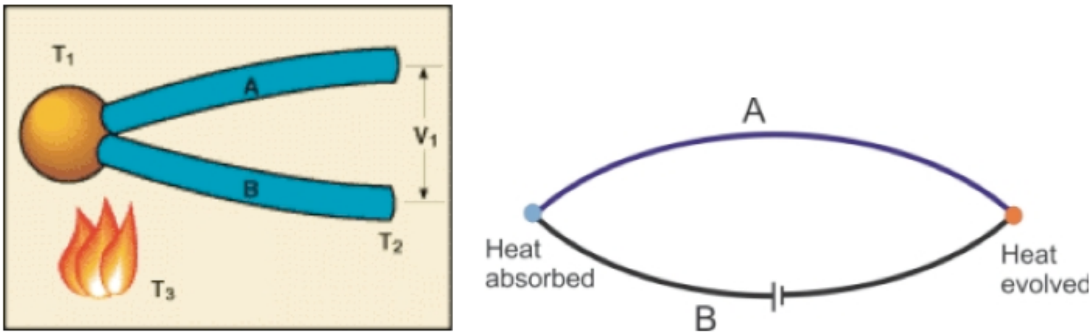

a) b)

Figure 1. Schematic of a) Seebeck effect and b) Peltier effect [1].

Conversely, the Peltier effect is the appearance of a thermal difference due to the applied voltage potential (Figure 1b). The ratio of the applied heat (q) and the electrical current produced (I) is defined as the Peltier coefficient:

$$\pi = \frac{q}{I}$$

The thermoelectric efficiency of a material is evaluated by its figure of merit zT. The higher the zT value, the better the thermoelectric performance of the material.

$$zT = \frac{\alpha^2 \sigma}{\kappa} T$$

where α: Seebeck coefficient (VK^{-1})
σ: electrical conductivity ($S.m^{-1}$)
κ: thermal conductivity ($Wm^{-1}K^{-1}$)
T: temperature (K)

The Seebeck coefficient (whose absolute value demonstrates thermopower) is given by:

$$\alpha = \frac{8\pi^2 k_B^2}{3eh^2} m^* T \left(\frac{\pi}{3n} \right)^{2/3}$$

where n : carrier concentration
m^*: effective mass of the carrier

Electrical conductivity:

$$\sigma = ne\mu$$

where μ is carrier mobility

Thermal conductivity originates from electrical carriers and lattice vibrations and is given by:

$$\kappa = \kappa_e + \kappa_l$$

κ_e: heat transported by electrical carriers ($\kappa_e = ne\mu LT$; L: Lorenz factor)
κ_l: heat transported by phonons.

A good thermoelectric material has high Seebeck coefficient, high electrical conductivity concurrent with low thermal conductivity. However, there is a trade off among these factors. The interrelationship between them is shown in Figure 2. The Seebeck coefficient is maximized when the carrier concentration is low (corresponding to insulators and semiconductors) and the charge carrier effective mass is high. Furthermore, only one type of carrier is wanted, otherwise generated potential caused by both electrons and holes under temperature difference will cancel each other. High carrier effective mass results in low electrical conductivity, which is unexpected in order to have large zT. Thus, optimizing the trade off between thermal and electrical conductivities is the challenge to achieve high performance thermoelectric materials [2].

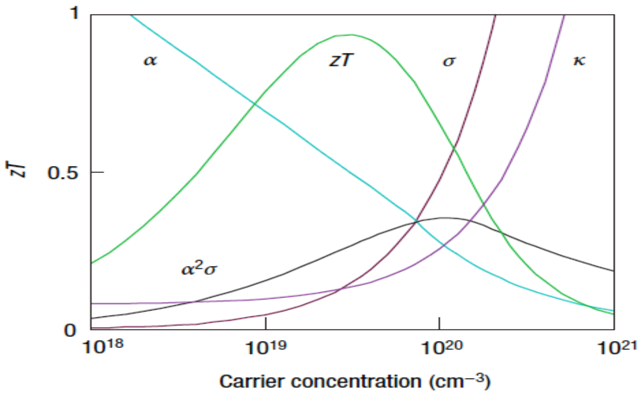

Figure 2. Dependence of zT, electrical conductivity σ, thermal conductivity κ, Seebeck coefficient α, thermoelectric power $\sigma^2\alpha$ on carrier concentration [2].

2.2. Thermoelectric materials

The thermoelectric effects have been discovered during the first half of the nineteenth century, however practical implication of thermoelectrics is still not as broad as its potential. This is because the conversion efficiency of conventional thermoelectric materials is low. Not until the mid 1990s there is a renaissance of interest for thermoelectrics due to a new prediction that nanostructural engineering can enhance performance of thermoelectric materials [3]. In the following the basic theory for improvement will be discussed.

2.2.1. Concepts for enhanced thermoelectric materials

As mentioned above, a good thermoelectric material has to possess high Seebeck coefficient, high electrical conductivity and low thermal conductivity at the same time. Figure 3 shows the figure of merit vs. temperature of some bulk thermoelectric materials. Metals own high electrical conductivity but also high thermal conductivity. Insulators are vise versa. Semiconductors are promising for optimization of thermoelectric performance. Because thermal conductivity originates from two sources: electrical carriers and phonons, it is possible to reduce thermal conductivity with insignificant influence to electrical conductivity [3].

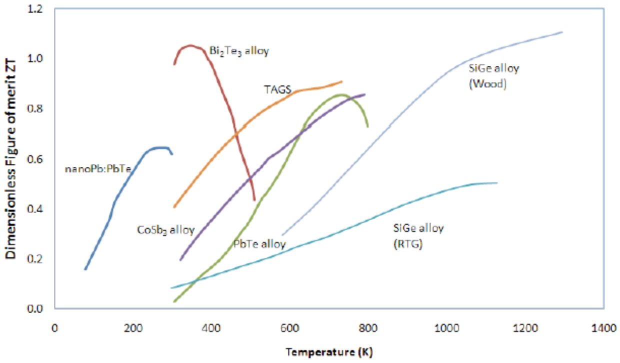

Figure 3. Dimensionless figure of merit ZT at different temperature ranges of conventional materials [3].

The figures of merit of different materials peak in different temperature ranges. Accordingly each thermoelectric material has its own application ranges. They can be classified as low temperature materials (200K-400K), medium temperature materials (400K-800K) and high temperature materials (above 800K) [3]. *z*T of 3 or above is necessary in order to achieve thermal-to-electric conversion efficiency comparable to the current widely used power generation technologies. Most attractive solutions to high *z*T are utilization of materials leaning towards phonon glass - electron crystal type, nanostructured materials and combination of both.

A basic theory for the first solution is that in materials that have cage-like structure (host) where a weakly bound atom or molecule (guest) resides, lattice phonon transport will be damped dramatically while electrical transport still remain almost unchanged. The guest is called rattlers. This feature exists in systems like skutterudites, clathrates and Zintl phases [3, 4].

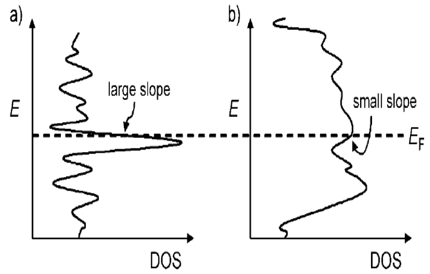

Figure 4. Hypothetical density of state with a) a large slope (d lnσ(E)/dE) and b) a small slope near E_f [5]

It is reported that there are two mechanisms of interest for nanostructured materials: quantum confinement and multi-interfacial effects. In the first one, new nanoscale phenomena reveal (such as changing density of states, metal-semiconductor transition) thus make it more probable to independently control interrelating factors: Seebeck coefficient, thermal conductivity and electrical conductivity. As the dimensions decrease, the electron energy bands in a quantum confined structure narrows, resulting in a high effective mass and therefore large Seebeck coefficient [2, 5]. Also, it is calculated that the maximum attainable figure of merit is:

$$S = \frac{\pi^2}{3}\frac{k^2 T}{e}\frac{d\ln\sigma(E)}{dE}\bigg|_{E=E_f}$$

where *σ(E)* is the electronic conductivity determined as a function of the band filling or Fermi energy E_f. If electronic scattering is independent on energy, then *σ(E)* is just proportional to the density of states at *E* (Figure 4) [5].

In the second mechanism, interfaces play a role of low energy carrier filters. First, in nanometer structure, phonons whose mean free paths are in the range of micrometer undergo ballistic transport in the system. Phonon-phonon scattering that dominates macrostructure becomes negligible whereas scattering from surfaces, dislocations, interfaces and other structural imperfections can dominate [6]. At such transition position, there exists a potential barrier that lets only high energy carriers pass through. Lower energy range of phonons than that of electrons makes phonons more susceptible to be scattered away (Figure 5) [4, 8]. There are plenty of ways to make interfacial structures: employing polycrystalline microstructure, aligning grains preferentially along favorable transport directions, reducing grain size, nanocoating grains, embedment of nanoinclusions and creating lamellar/multilayer structure (Figure 6) [7].

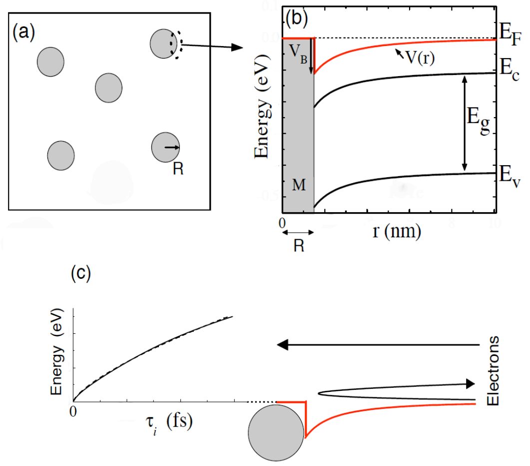

Figure 5. Schematic of semiconductor host with metallic nanoinclusions. The red line shows the energy at the interface between nanoinclusions and the host. Low energy electrons are bounced back at the interface potential but high energy electrons are unaffected [6].

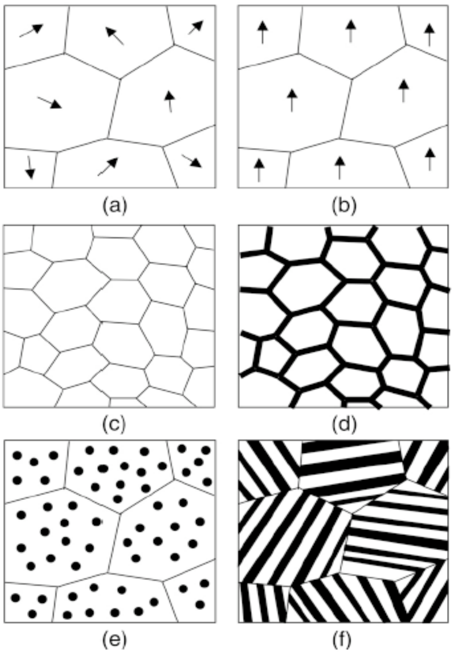

Figure 6. Strategies for improving bulk thermoelectric performance employ several distinct classes of grain and interfacial microstructure. (a) A polycrystalline microstructure. (b) Preferential alignment of grains along favorable transport directions. (c) Reduced grain size to take advantage of favorable interfacial scattering processes. (d–f)Nanocomposites: (d) nanocoated grains, (e) embedded nanoinclusions, and (f) lamellar/multilayer structures [7].

Reducing grain size and using nanoinclusions are the strategy of investigation in this work.

2.2.2. Thermoelectric materials

Conventional thermoelectric materials include some metals (Cu, Fe, NiCr alloys, Pt) for thermocouples; Bi_2Te_3 for cooling; SiGe, bismuth telluride, PbTe for electricity generation [1]. However these materials have low thermal-electrical conversion efficiency. During the last decade, there has been renewed interest in the search for improved thermoelectric materials. Some typical ones are:

Skutterudites

Skutterudite materials have compositions of MX_3 where M = (Co, Rh, Ir) and X = (P, As, Sb). They have large unit cells and a cage-like structure. The cage-like structure makes it possible to incorporate guest atoms (of another element) that can play a role of phonon-scattering centers by acting as "rattlers". Meanwhile these atoms do not deter the motion of electrical charge in the system. Some possible elements that can be used as rattlers in the system are lanthanum families, thallium, actinide, alkaline-earth, alkali, and group IV elements. Firgure 8 shows the figure of merit of some skutterudites.

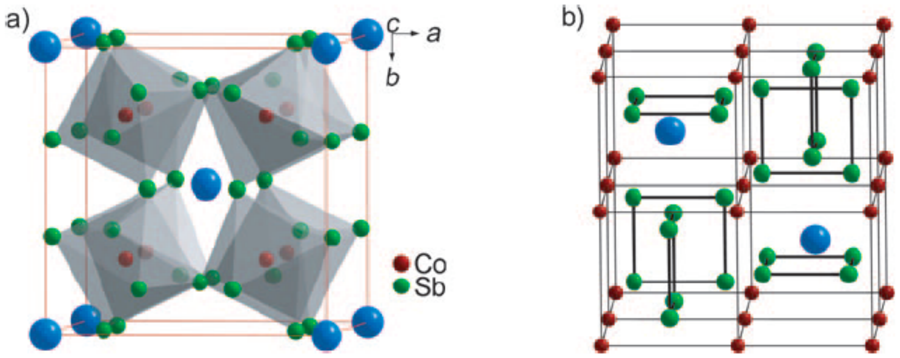

Figure 7. Two model structures of the Skutterudite ($CoSb_3$) a) Unit cell of skutterudite. Sb form octahedral cages in which Co atoms reside. The voids formed by Co and Sb are filled with guest atoms symbolized by big blue spheres. b) The model is shifted by the fractional coordinates ¼. ¼. ¼ from the unit cell [5].

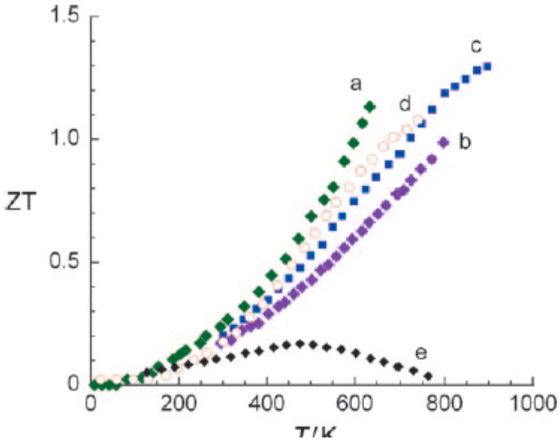

Figure 8. zT of some Skutterudites [5].
a) $Yb_{0,19}Co_4Sb_{12}$,
b) $Ca_{0,18}Ni_{0,03}Co_{3,97}Sb_{12,4}$,
c) $Ba_{0,3}Ni_{0,05}Co_{3,95}Sb_{12}$,
d) $Ce_{0,9}Fe_3CoSb_{12}$, e) Co_4Sb_{12}

Clathrates

Clathrates, being the main topic of this thesis, are promising thermoelectric materials. Because this is the material of investigated in this work, more details about them will be given in section 2.2.3

Half Heusler

The general formula for half Heusler intermetallic compounds is MNiSn (M= Ti, Hf, Zr). Half Heusler phases consist of three filled interpenetrating fcc sublattices and one vacant sublattice. Optimization of thermoelectric properties of this compound can be done by chemical modification. They have large room temperature Seebeck coefficient and high electrical conductivity.

Figure 9 shows the figure of merit of some typical thermoelectric materials, including $Ba_8Ga_{16}Ge_{30}$ clathrate – the object of this thesis.

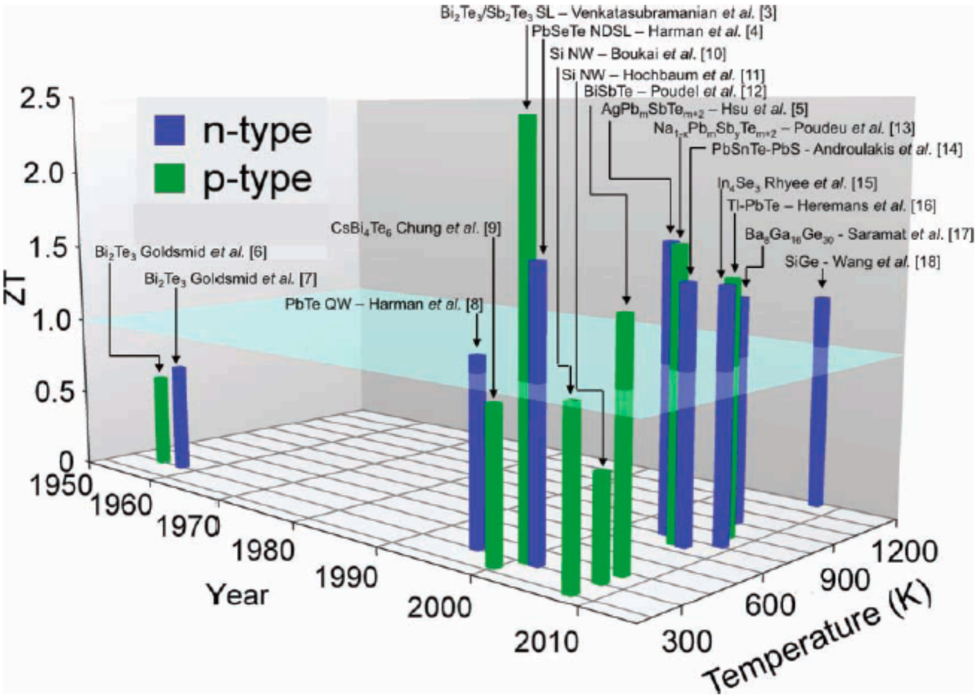

Figure 9. Figure of merit zT of state-of-the-art materials as a function of temperature and year illustrating important milestones [8].

2.2.3. Clathrates

Thermoelectric clathrates is one type of materials that follow phonon glass – electron crystal concept. Clathrate is defined as “an inclusion complex in which (neutral) molecules of one substance are completely enclosed in cavities formed by the crystal lattice or are present in large molecules of another substance, i.e. the crystal takes in foreign molecules during growth, which cannot escape until the crystal is decomposed" [9]. It is expected that there is no direct bonding between guest and framework atoms but there exist an interaction between them, where the guest atoms play a role of charge donors following the Zintl concept.

In terms of crystal structure, there are two types of clathrates that have received most attention for thermoelectrics [5]:

- Type I: unit cell has cubic structure and holds 46 group IV atoms. They can be $X_2Y_6E_{46}$ and $A^{II}_8B^{III}_{16}B^{IV}_{30}$ (eg. Na_8Si_{46}, $Ba_8Ga_{16}Ge_{30}$, $Ba_8Ga_{16}Si_{30}$) X,Y: guest atoms encapsulated in two different polyhedral cages E_{20} and E_{24} (E: tetrahedrally coordinate framework atoms) (Figure 10 - top)
- Type II: unit cell also has cubic structure, but contains 136 atoms that form dodecahedron and hexakaidecahedron cages. (Figure 10 - bottom)

The subject of this work is type I clathrate composed of Ba, Ga and Ge whose crystal structure is shown in Figure 11. Its general formula is $Ba_8Ga_{16+x}Ge_{30-x}$. In this structure, varying the ratio between host atoms results in the tuning of electrical properties, that is, control the doping of the material (p-type or n-type). Ba atoms act as donors whose electron carriers are compensated by Ga. Thus, the by controlling the Ga composition, carrier concentration and the carrier type of $Ba_8Ga_{16+x}Ge_{30-x}$ clathrate can be tuned. Depending on the value of x, the material is p-type (x>0) and n-type (x<0) [11,12,13].

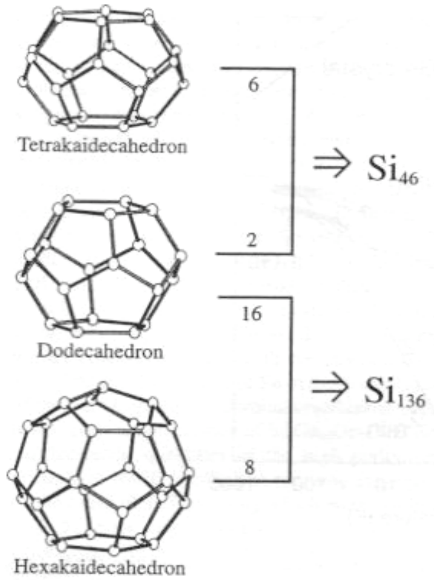

Figure 10. The polydehral building blocks of type I (top) and type II (bottom) clathrates [10].

Figure 12 shows the figure of merit of $Ba_8Ga_{16+x}Ge_{30-x}$ synthesized by Czochralski method as a function of temperature. With zT = 1,35 at 900 K and extrapolated climax value of 1,63 at 1100K, the material has a potential for large scale applications at high temperature such as power generation [14].

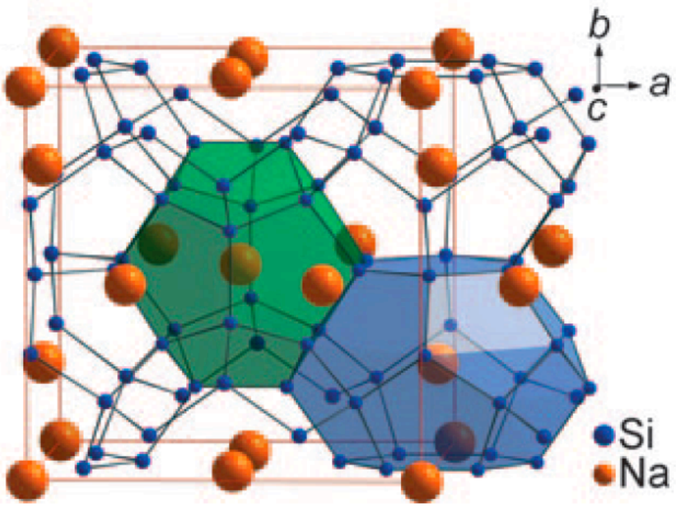

Figure 11. Crystal structure of clathrate type 1. Different cages are formed: tetrakaidecahedral (blue) and pentagonal dodecahedral (green) [5].

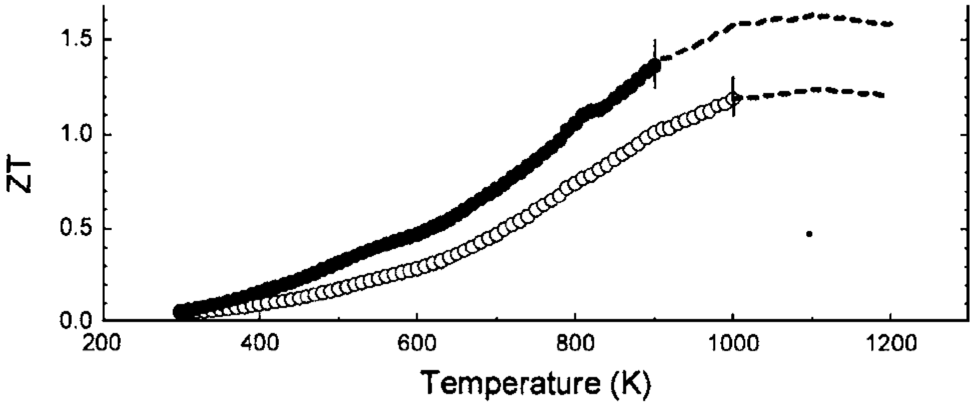

Figure 12. Figure of merit zT as a function of temperature for $Ba_8Ga_{15,31}Ge_{30,48}$ *(white spheres) and* $Ba_{7,94}Ga_{15,33}Ge_{30,67}$ *(dark spheres) clathrates synthesized by Czochralski method and their extrapolation up to 1200K (dashed line) [14].*

Chapter 3

Experimental method used

3.1. Sample preparation

The goal of this work is to investigate the influence on thermoelectric performance of introduction of gold particles into bulk clathrate and the effect of their particle sizes. The following is an outline of the preparation steps:

1. Gold colloids with different particle sizes
   - 4 gold solutions with 4 different particle sizes (5, 8, 17, 37 nm) and narrow size distributions were made.
   - Gold suspensions were subjected to purification and drying process:
     - First, filtration was used to primarily filter sedimented excess surfactant. The excess surfactant is unwanted in the final gold suspensions.
     - Second, the suspensions were concentrated to the volume of 1:10 compared to that of initial solutions using rotary evaporation method to remove water. After that, all solutions were subjected to ultracentrifugation two times to sediment gold particles and further remove excess surfactant because it acts as impurity in the final sample.

2. Synthesis of clathrate $Ba_8Ga_{16}Ge_{30}$

   Clathrate $Ba_8Ga_{16}Ge_{30}$ powder was made by heat treatment of a mixture of pure Ba, Ga and Ge elements at predetermined composition. Then, the obtained bulk compound was ground into fine powder and was then divided into 6 equal portions.

3. 6 samples were prepared

   A reference clathrate material free of gold was prepared to be able to assess the effect of the nanoinclusions. Five materials were prepared by mixing 8 g clathrate powder with $10{,}693 \times 10^{-3}$ g gold particles in colloid state using the four different gold suspensions prepared (See Table 1). The values were chosen so that the volume ratio of gold to clathrate is 0,4%. This ratio was reported to be optimal in a similar study, in which TiO_2 was used as nanoinclusions [15].

4. Freeze drying the materials prepared in step 3.

5. Heat treatment of materials obtained from the 4th step to decompose the remaining surfactants in the system.

Material ID	A	B	C	D	M	REF
Gold particles size (nm)	5	8	17	37	5, 8, 17, 37 (equal in mol)	No gold
Clathrate (g)	8	8	8	8	8	8

Table 1. Recipe for materials prepared.

6. Samples after heat treatment were subjected to compression by spark plasma sintering.

In the following, details of each step will be described.

3.1.1. Gold nanoparticle colloids

To prepare colloidal suspensions of gold nanoparticles with narrow size distributions but with different particle sizes, the synthesis process reported in [16] was used. The method is a seeding and growth method.

Chemicals used were: trisodium citrate (≥ 99%, Sigma-Aldrich), chloroauric acid ($HAuCl_4.3H_2O$) (99%, Sigma-Aldrich), ascorbic acid (≥ 99%, Sigma-Aldrich), sodium borohydride ($NaBH_4$) (99%, Sigma-Aldrich) and cetyltrimethylamonium bromide (CTAB) (≥ 99%, Sigma-Aldrich).

4 gold suspensions A, B, C, D with expected particles sizes of 5, 8, 17, 37 nm, respectively were made (Table 2).

According to the calculated amount of gold needed for each thermoelectric material, the amounts of each solution A, B, C, D that had to be prepared were 1040 ml, 670 ml, 410 ml, and 360 ml, respectively. The recipe for making this much solution was scaled up from the recipe that was originally for every 10 ml of each solution. In the following the recipes for 10 ml of each solution are given.

1. Preparation of seed solution

   $HAuCl_4$ and $Na_3C_6H_5O_7$ were diluted in de-ionized water to the concentration of $2,5x10^{-4}$ M. 0,1 M $NaBH_4$ solution was then prepared. 0,6 ml of freshly made, ice-cold $NaBH_4$ solution was added dropwise into 20 ml prepared solution of $HAuCl_4$ and $Na_3C_6H_5O_7$. $NaBH_4$ reduces $HAuCl_4$ immediately after being added to the gold salt solution and form gold seed. At room temperature, $Na_3C_6H_5O_7$ cannot reduce gold salt and acts as capping agent. The necessary volume of seed solution was too large (1040 ml*)*, it is impossible to prepare all at once. Otherwise, because the reduction reaction happened very fast, newly reduced gold will aggregate to previously formed gold particles and results in larger gold particles, which was undesired. For this reason, 13 separate 80ml-batches of seed solution were made instead of a big batch of 1040 ml.

2. Preparation of growth solution

   In total, the amount of growth solution required was 1380 ml. For each 100 ml of growth solution, 100ml of 2,5x10^{-3} M $HAuCl_4$ solution was made. After that, 3 gram CTAB was added into it. The obtained growth solution was stirred and heated to 50°C for the surfactant to dissolve completely. Then, growth solution was naturally cooled to room temperature. At this state it had reddish-orange color.

3. Preparation of gold suspensions A, B, C, D and M

   Recipes for solutions A, B, C and D are shown in Table 2. For solutions A and B, seed solutions used were the as-prepared seed solution. Within 40 minutes of their synthesis, part of solutions B and C were used as seeds for solutions C and D, respectively. The volume of gold solutions were chosen so that in each prepared solution there was 5,43×10^{-4} mol of gold. This gold will amount to 0.4% volume of final materials after mixing with clathrate.

	Seed solution (ml)	Growth solution (ml)	Ascorbic acid solution (freshly made) (ml)
A	2,5	7,5	0,05
B	1	9	0,05
C	1 (Seed: solution B)	9	0,05
D	1 (Seed: solution C)	9	0,05

Table 2. Recipes for solutions A, B, C and D.

Solution M was a mixture of solutions A, B, C, D, each contributing the same mol of gold.

4. Surfactant filtration

   Prepared solutions A, B, C, D and M still contained much residual surfactant that precipitated visibly. Surfactant should be removed because it would be impurity and we want only gold particles mixed with the clathrate powder.

   Surfactant molecules in the solutions exist in 3 states: immiscible, miscible (at 25°C, the solubility of CTAB is 1,5 grams per 100 ml) and capped onto gold particles.

   To decompose CTAB that surrounded gold particles, heat treatment, was performed when mixture of gold and clathrate in powder form was obtained, as a later stage. There were 3 steps used to remove the CTAB in solutions. First the precipitated CTAB was filtered with filter paper (mean pore size: 1 μm). After the first filtration, solutions were subjected to rotary evaporation, during which they were concentrated to 10 times. Again, surfactants precipitated in concentrated solutions were removed by using filter paper. By that, most insoluble CTAB was removed. In order to eliminate soluble CTAB, ultra centrifuge was the next step to process on all obtained concentrated solutions. This step was repeated 2 times, after which the final solutions were ready for mixing with clathrates.

5. Rotary evaporation

In order to make a good nanoinclusion in clathrate, it is necessary to disperse clathrate powder very well into gold solution. The volume of each gold solution needed for each final sample was very high as mentioned above. It is difficult to disperse 8 grams of clathrate into that much solution and then process the mixture to make all of them become powder again. It necessitates concentrating the gold solutions. The process must be performed in such a way that it does not influence the gold particles' size in the solutions. Rotary evaporation was chosen as the primary step for this procedure.

A rotary evaporator is an equipment that can remove water gently from a solution. The basic principle of rotary evaporation is that the boiling temperature of the liquid content in the solution can be lowered by lowering the pressure above the solution's surface. By that, water can be removed with less dramatic thermal influence to the other contents in the solution and after all the solution is concentrated.

Each prepared gold solution was heated to 75^{o}C under low pressure to evaporate water. The solutions after rotary evaporation were 10 times more concentrated than before (that is, their volumes were reduced 10 times).

6. Ultra-centrifugation

Rotary evaporation could only remove water from the gold solutions. There was still a large amount of surfactant molecules remaining in the solution. Part of them formed sediment after the solution had cooled naturally to room temperature. Other surfactant molecules were dissolved in the solution and capped around the gold particles.

In order to separate substances of different densities in a mixed solution, centrifugation is a popular and effective method. A centrifuge spins liquid samples at high speed, facilitates the downward movement of denser material due to gravitational force. As an object is spinning, there is a centrifugal force that pushes the denser objects outwards from the spinning center. The amplitude of the force is:

$$F= m\omega^2 r$$

Where m: object's mass; ω: angular velocity; r: the distance of the object from the spinning center.

Thus, objects with larger density will experience greater force and tend to move faster to the outer edge of the container than ones with lower density.

After centrifugation, substance with higher density will sediment to the bottom of the centrifuge tube and thus be separated [17].

The Beckman Coulter ultracentrifuge was the equipment used for this step. It can rotate at the maximum speed of 90000 revolutions per minute. During operation there is vacuum in rotation chamber to reduce the friction with air and to maintain the temperature of the material in the ultracentrifuge tube constantly at preset value. The ultracentrifuge tube used was a thin wall polyallomer.

The purpose to perform ultracentrifugation on gold solution was to remove soluble surfactant from the solution. After ultracentrifugation, gold nanoparticles that were denser than surfactant micelles deposited at the bottom and formed very dense bottom layer containing mostly gold particles. Only that part was kept for the second ultracentrifugation.

Each gold solution A, B, C, D and M was ultracentrifuged two times. Obtained solutions after rotary evaporation were filled into 8 ultracentrifuge tubes. Each tube has the volume of approximately 8,9 ml. Spinning speed was set at 20 000 rpm for B, C, D, M. For A the spinning speed was set at 30 000 rpm because the average particle size was smaller than that of B, C, D, M. Otherwise there were still some gold particles that did not sediment to the bottom of the centrifuge tube. Spinning time was 45 minutes. Temperature inside tubes was held at 22°C to prevent surfactant from precipitating from the solution and form big crystals that also deposit to the bottom together with gold particles. Milli-Q water was used to redisperse obtained gold particles after each ultracentrifugation step.

3.1.2. Clathrate

Three batches of polycrystalline $Ba_8Ga_{16}Ge_{30}$ clathrate were synthesized by direct reaction of high purity elements Ba, Ga and Ge (≥ 99%, all from Aldrich). For every 18 grams of clathrate made each time, the weight of Ba was 4,5844 g, Ga was 4,4848 g and Ge was 8,9308 g. The elements were put in a Al_2O_3 crucible and sealed in a quartz tube. With those weights, the chemical formula of the prepared clathrate was $Ba_{8,2}Ga_{15,8}Ge_{30,2}$.

The reaction crucible was heated slowly for 8 hours to 1050 °C so that all elements could melt and react with each other and form $Ba_8Ga_{16}Ge_{30}$ clathrate. The melted mixture was kept at 1050 °C for 1 h for exhaustive reaction, then the crucible was cooled to 980 °C over 6 hours. The next step was a 4 hours decrease in temperature to annealing temperature 963 °C, which is just below the melting temperature of the clathrate. The annealing time was 24 hours so that the clathrate crystals could grow and homogenize. Again the crucible was controllably cooled to 930 °C in 4 hours, followed by a 9 hours cooling to room temperature [18].

After synthesis, the prepared clathrate batches were pre-ground by Mixer Mill (MM400 from Retch) for (40 minutes at 15 Hz). Then, every 9 grams of obtained powder were ground finely at frequency of 16 Hz for 40 minutes. The whole obtained powders were mixed together before dividing them into 6 portions of 8 grams.

3.1.3. Mixing gold colloids with clathrate

After processing the gold solutions of different particle sizes, the next step was to mix them with clathrate powder.

6 samples were made, 5 of them were mixed with gold nanoparticles for investigation and one was the pure clathrate sample (no mixing with gold nanoparticles) that was used as reference. 5 portions of clathrate powder, each weighing 8 grams were put into 5 solutions of gold nanoparticles A, B, C, D and M. The reference sample is denoted REF.

The clathrate powder was put into conical flasks and gold solutions were poured into them. Then the mixture was shaken vigorously so that the clathrate powder could disperse evenly in the solution. Then the mixture was rapidly frozen in a state that particles were distributed evenly in the solution so that in the next step: drying, the gold particles could blend well into clathrate powder. This step was done by dipping the whole conical flask into liquid nitrogen while rotating it fast by a drill until the solution was totally frozen.

The frozen mixtures were then subjected to freeze-drying during which water would sublimate from the ice by low pressure and yield in a mixed powder of clathrate and gold particles. The freeze-drying took 2 days to finish.

3.1.4. Freeze drying

Freeze drying is a drying process which consists of removing water from a frozen sample by sublimation and desorption under vacuum. The principle underlying this method can be illustrated by the phase diagram of water (Figure 13). At low temperature and low pressure, material can transform from solid to gas without becoming liquid phase. In freeze-drying, the sample is cooled down to temperature below triple point at which the solution is solidified. Then the pressure will be decrease so that the solid water in the solution can sublimate and results in water-free sample [19].

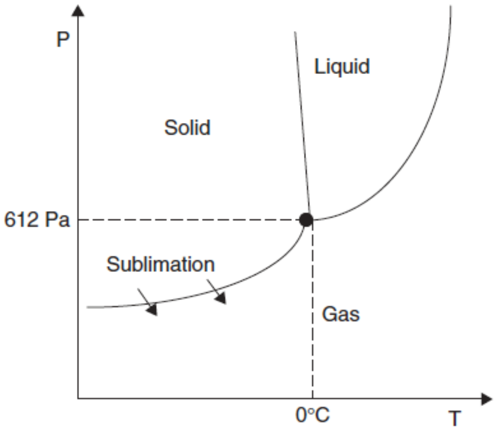

Figure 13. The phase diagram of water [19]

3.1.5. Heat treatment

As mentioned above, in the final powder mixture of gold and clathrate, there is still CTAB as impurity that capped onto gold particles. To get rid of them, heating of the powder obtained from freeze-drying was carried out. The samples were heated to 350 °C and kept at that temperature for 4 hours. The temperature needed for the degradation of CTAB was determined by using thermogravimetric analysis.

3.1.6. Compaction by spark plasma sintering

The final powder samples after heat treatment were compressed into tablets by the spark plasma sintering technique. This step was done in Department of Inorganic Chemistry, Arrhenius Laboratory, Stockholm University.

Spark plasma sintering, also known as Field Assisted Sintering Technique or Pulsed Electric Current Sintering, is a sintering technique that is gaining increasing popularity for making thermoelectric nanocomposites. In the spark plasma sintering technique, heat is generated locally and internally, in contrast to conventional hot pressing in which external heating elements are used. In this technique, a pulsed electric current is used to form good contacts between particles in powder sample. As a pulsed current flows through the powder sample, at the small gaps between particles, electrical discharges form. These discharges generate microscopic electric arcs that form local high temperatures and pressures, which weld particles in the powder sample together. Conventional densification routes have the disadvantage of coarsening material. But with fast and extreme conditions formed in-between particles, spark plasma sintering can solve this problem and it also becomes a fast technique [3].

3.2. Sample characterization

3.2.1. X-ray Diffraction (XRD)

The X-ray diffraction (XRD) technique was used to characterize the crystal structure of obtained clathrate powders. In XRD, a collimated beam of X-rays with a wavelength typically ranging from 0,7 to 2 Å, is incident on a specimen and is diffracted by the crystalline phases in the specimen according to Bragg's law [20]:

$$n\lambda = 2d\sin\theta$$

Where d: the spacing between atomic planes in the crystalline phase
λ: the X-ray wavelength.
θ: the angle between incident and reflected beam.

When an electromagnetic beam is incident to an object, it scatters. So an X-ray when it is incident on a crystal structure of atoms and electrons. Because the wavelength of incident X-ray is of the same length scale to the periodicity of crystal structures, scattered rays are diffracted, and diffracted beam interferes. In case of constructive interference, diffraction pattern whose properties are dependent on the nature of crystal structure can be visualized. Only beams whose travel distance between the source and the detector is an integer multiple of wavelength interfere constructively. This is regarded as Bragg's condition. By analyzing the intensity and position of constructive interference points in diffraction pattern, the crystalline structure of the specimen can be revealed.

3.2.2. UV-Vis spectroscopy

Analysing ultraviolet - visible absorption spectrum of gold nanoparticles has been popularly used to determine the particle diameter [21]. This is an effect of surface plasmon resonance. When an electromagnetic field at a certain wavelength is irradiated to a nanoparticle, the field is confined onto small surface area of the nanoparticle, induces surface electrons and polarizes the particle, which leads to the creation of an additional electromagnetic field. As a consequence the electromagnetic field that the whole nanoparticle feels is the combination of incident and induced radiation.

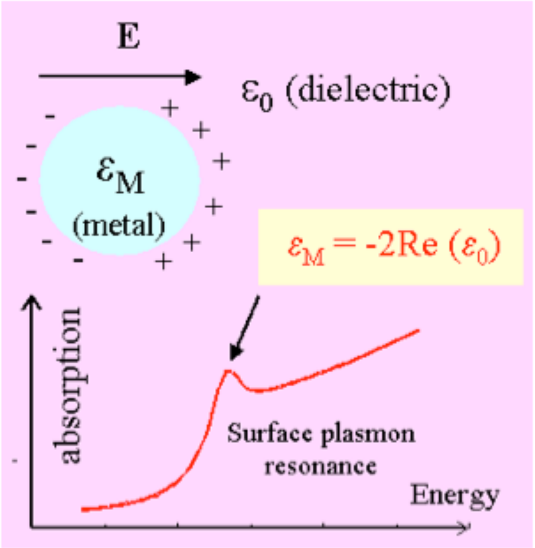

Figure 14. Surface Plasmon resonance of metallic nanoparticles. [22]

Provided a neutral metal sphere in a certain medium is irradiated by an electric field E_0. Dielectric function of the sphere: $\varepsilon_{sphere}(\omega)$ depends on incident frequency ω. Dielectric constant of the medium is ε_{medium}. The total field outside the sphere is the sum of induced field and incident field E_o (figure 14)

$$E_{total} = \frac{\varepsilon_{sphere}(\omega) - \varepsilon_{medium}}{\varepsilon_{sphere}(\omega) + 2\varepsilon_{medium}} \left(\frac{a}{r}\right)^3 E_0 + E_0$$

a: radius of the metal sphere, ω: frequency of incident radiation, and r: distance from the induced dipole.

The dipole p created in the sphere by external field:

$$p = \frac{\varepsilon_{sphere}(\omega) - \varepsilon_{medium}}{\varepsilon_{sphere}(\omega) + 2\varepsilon_{medium}} a^3 E_0$$

The induced dipole maximized when $\varepsilon_{sphere}(\omega)$ equals to $-2\varepsilon_{medium}$. At some particular frequencies the condition is satisfied (figure 15). Figure 15 shows dielectric function of gold and silver nanoparticles. From the figure it turns out that in visible irradiation range, the real part of dielectric function of the sphere approaches minus two times the dielectric value of the environment (either dielectric medium or air), which means that the induced dipole reaches its maximum. In other words, surface plasmon resonance appears, which can be shown in the absorption spectra. [22]

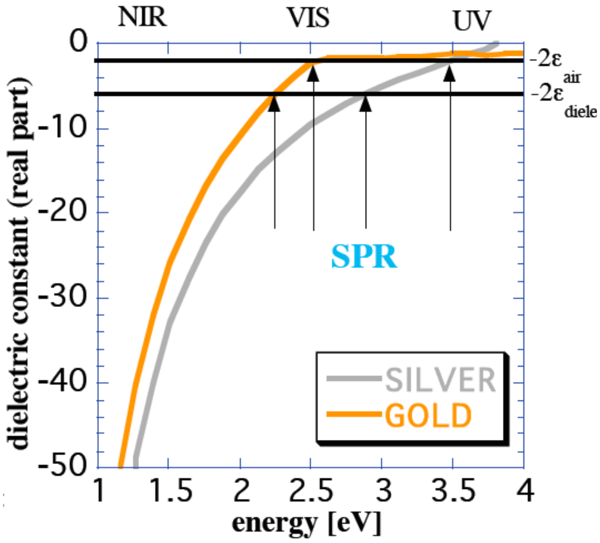

Figure 15. Dielectric function of gold and silver nanoparticles [22].

The position of the absorption peak is a function of sphere's radius. Thus it is possible to extract the gold particle's size from the absorption spectra.

The detailed theory on calculation of particle size from position of absorption peak are studied and reported in some papers [23,24]. In this work, the size of gold nanoparticles was estimated based on experimental data of another study [16].

3.2.3. Transmission electron microscopy (TEM)

In this study, transmission electron microscopy was used to determine the sizes of obtained gold particles.

In TEM, electrons are accelerated to 80 keV or higher (up to 1 MeV), projected onto a thin specimen through a condenser lens system, interacted with the specimen and penetrated outwards either undeflected or deflected compared to the initial path. Penetrated beam through the sample was then detected and formed a zoom-in image of the sample. Image formed by penetrated electron beams reveal information about sizes of the particles in the sample.

3.2.4. Dynamic Light Scattering (DLS)

The gold particle sizes were also determined by Dynamic Light Scattering technique.

Figure 16 shows a typical instrument setup for DLS. A laser beam from laser source passes through polarizer and attenuator before it is incident the sample, which is kept thermostable. The attenuator is used to adjust the intensity of incident beam according to strong or weak light scattering sample so that the intensity of the detected beam is in the operation range of the detector. Part of the incident beam will transmit through the sample. Part of it scatters by the particles in the sample at all angles. Scattered light is detected by a detector where a light intensity is obtained by counted photon events. The signal of scattered light is sent to a correlator to be processed. The correlator compares the intensity of the scattered light after consecutive time intervals to derive the varying rate of the intensity. The data is analyzed by computer software to derive information on particle size.

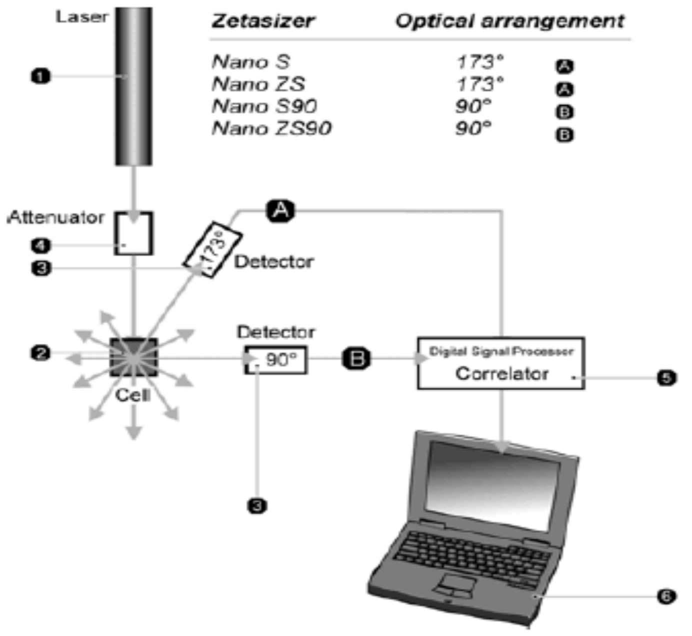

Figure 16. Schematic of dynamic light scattering system [25].

In a solution, particles collide randomly to each other and to solvent molecules. These collisions are controlled by thermodynamics of the solution and cause random movement (which is called Brownian motion) of the particle in the solution. Consequently, the particles are kept suspended in the solution without precipitation. The diffusion rate of a solution at a given viscosity and constant temperature is inversely proportional to the particles' sizes. Diffusion coefficient of the particles in solution is given by the Stokes-Einstein equation:

$$D = \frac{k_B T}{3\pi\eta d}$$

Where k_b: Bolzmann constant (1,38 x 10^{-16} erg/K)

T: temperature (K)

η: solvent viscosity (poise)

d: equivalent spherical diameter (centimeters)

By measuring the diffusion coefficients, it is possible to derive the size of particles in solution. Note that the diffusion coefficient not only depends on the core of the particle but also dramatically depends on its shape and surface, as well as the nature of the solvent. Thus the diameter measured is the diameter of a sphere that has the same translational diffusion coefficient as the particle [25].

The particles in solution are illuminated by a laser beam. At any given instant, light scattered by particles, which experience Brownian motion, adds together to form an interference pattern whose intensity is detected by a PMT (Figure 16). Thus the movement of particles in the solution influences the intensity of light detected at the PMT. As the movement is random, their relative position to each other changes, consequently the interference pattern changes constantly and varies the light intensity at the detector. Large particles move slowly thus yield a slow intensity alteration at the detector. On the other hand, small particles cause rapid intensity fluctuation. DLS measures the exact time scale of random intensity fluctuations (Figure 17) at the detector to process the information on particles' sizes. [25]

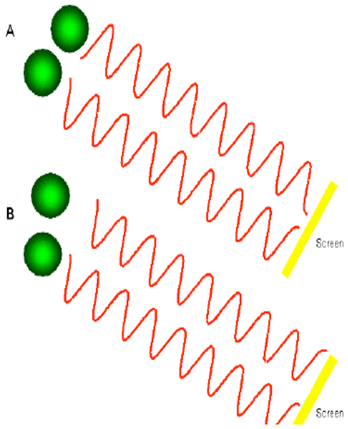

Figure 17. The observed signal depends on the phase addition of the scattered light falling on the detector. A: two beams interfere and cancel out each other. B: two beams interfere and enhance each other [25].

The displayed results will be the distribution of particles sizes in three forms: intensity, volume and number distributions whose peaks are proportional to the power of 6, 3, 1, respectively of particles diameter. (Figure 18) [25]

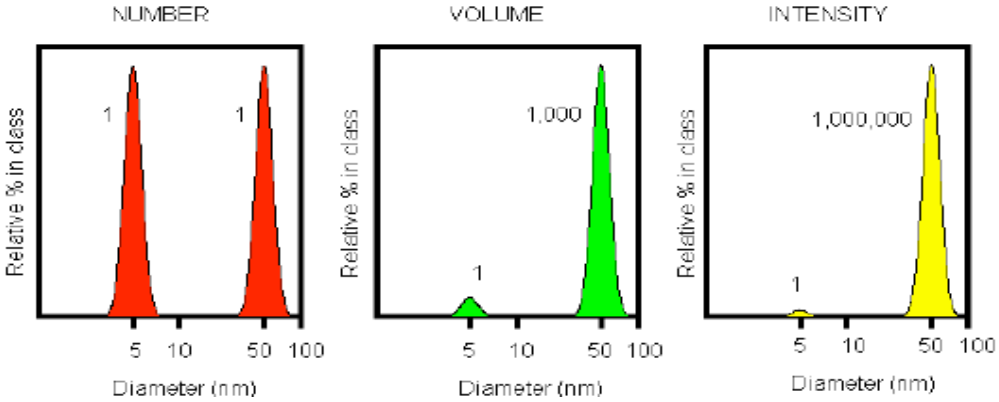

Figure 18. Number, volume and intensity distribution of a bimodal mixture of 5 and 50 nm lattices present in equal numbers [25].

In this work, the measurement was carried out by equipment named N4 Plus. The N4 Plus determines particle size by measuring the rate of diffusion of particles through a fluid. If the temperature and viscosity are known, the particle size can be calculated.

DLS measurements for each sample were repeated at least 5 times. Only reliable results were used. The averages of obtained reliable results were calculated.

3.2.5. Thermogravimetric analysis (TGA)

Thermogravimetry is a versatile technique with capability of analyzing compositions, determining degradation temperatures and rate of degradation of substances in a mixture and the thermal stability. In this method, changes in weight of material are traced with changes in temperature applied on it. Figure 19 is a schematic of the equipment. A small amount of material is put into a pan, which is attached to a microbalance. The whole thing is put into an electrically heated furnace. Temperature in the furnace is controlled to follow a preset temperature program. The temperature of the sample is measured by a thermocouple. The atmosphere in the furnace can be air (for oxidation analysis) or inert gas [26].

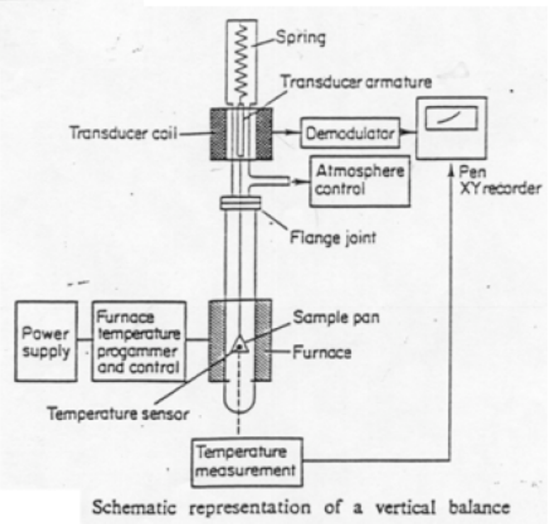

Figure19. Schematic of TGA [26].

In this work, TGA was used to determine the temperature range in which CTAB was degraded so that the final sample became free of CTAB. 8 miligrams of gold-clathrate powder, i.e., sample after freeze drying was used for thermogravimetric analysis. The temperature program was: (1) increase temperature from room temperature to 350 °C at the rate of 1°C/min, (2) kept temperature constant at 350 °C for 4 hours, and (3) cooled down the temperature from 350 °C to room temperature at the rate of 1 °C /min. The temperature program was chosen based on a published report [27].

3.2.6. Thermal conductivity measurement

After the compressing step, tablet-like samples were obtained and were subjected to thermal conductivity measurements. The measurements were carried out using a Hot Disk equipment. The Hot Disk measures thermal conductivity based on the transient plane source (TPS) technique. The transient plane source element simultaneously plays a role of heat source and temperature sensor.

In this technique, the sensor will be sandwiched between two pieces of sample whose surfaces are flat so that the sensor could be approximated as a planar heat source. A pulsed electrical current is generated in the sensor and the produced heat propagates into the sample. At the same time, the change in temperature in the sample results in the change in resistivity of the sensor, which can be recorded by the voltage variation over the sensor. It is noted that heat generated by the pulsed electrical current should not reach the boundaries of the sample and it can be approximated as propagating through an infinite environment. To achieve this, firstly the length of pulsed current should be short enough so that the consequent heat dissipates only within the sample. Secondly, the intensity of the pulse current should not be either too high or too low. Also, the conductive core of the sensor should be covered with good thermal isolating material to reduce the heat loss to the surrounding [28].

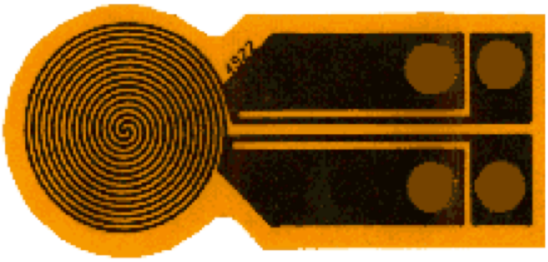

Figure 20. Hot disc TPS [29]

Besides the length and intensity of the pulse electrical current, the sensor's geometry configuration, sensor's material, and the conductive pattern design on it also principally influence the measured thermal conductivity values and thus have to be carefully monitored. Typically the TPS elements are made of 10µm thick nickel foils embedded in 25 µm thick kapton or mica as thermal insulator. In figure 17 the hot disc design for TPS that was used in work is shown.

In this work, the TPS element was a mica sensor. The pulse electrical current was 90 mW and lasted for 2 seconds. Thermal conductivity of the 6 samples was measured at different temperatures: 22 °C, 100 °C, 200 °C, 300 °C, 400 °C, 500 °C and 600 °C.

Chapter 4

Results and discussion

4.1. $Ba_8Ga_{16}Ge_{30}$ clathrate

Figure 21 shows the XRD pattern of as-prepared $Ba_8Ga_{16}Ge_{30}$ clathrate powder (top) and final clathrate with gold nanoinclusion tablets (bottom). In the top pattern, characteristic peaks of $Ba_8Ga_{16}Ge_{30}$ are clearly shown. The sharpness of the peaks reveals high crystallinity of obtained $Ba_8Ga_{16}Ge_{30}$. Although the compositions of the elements before reaction shows the formula of $Ba_{8,2}Ga_{15,8}Ge_{30,2}$, the synthesized clathrate still becomes the $Ba_8Ga_{16}Ge_{30}$ phase as expected from previous experience showing that a slight Ba excess is beneficial for the synthesis in the XRD pattern.

After processing steps including mixing with gold solutions, heat treatment and spark plasma sintering, there was a change in sample's compositions. The XRD pattern of the final clathrate tablet from the sample C in the bottom picture suggests that there was a phase change from $Ba_8Ga_{16}Ge_{30}$ to $Ba_{7.76}Ga_{13.8}Ge_{31.84}$. This is likely due to the atmosphere and temperature condition applied during the spark plasma sintering. There was a loss of Ga during the sintering and it is believed to be the reason for the phase change. This $Ba_{7.76}Ga_{13.8}Ge_{31.84}$ stoichiometry is expected to be n-type clathrate.

Also, there was a formation of an oxide phase of Ba and Ga visible in the XRD. This could have happened during the heat treatment process employed to degrade the surfactant.

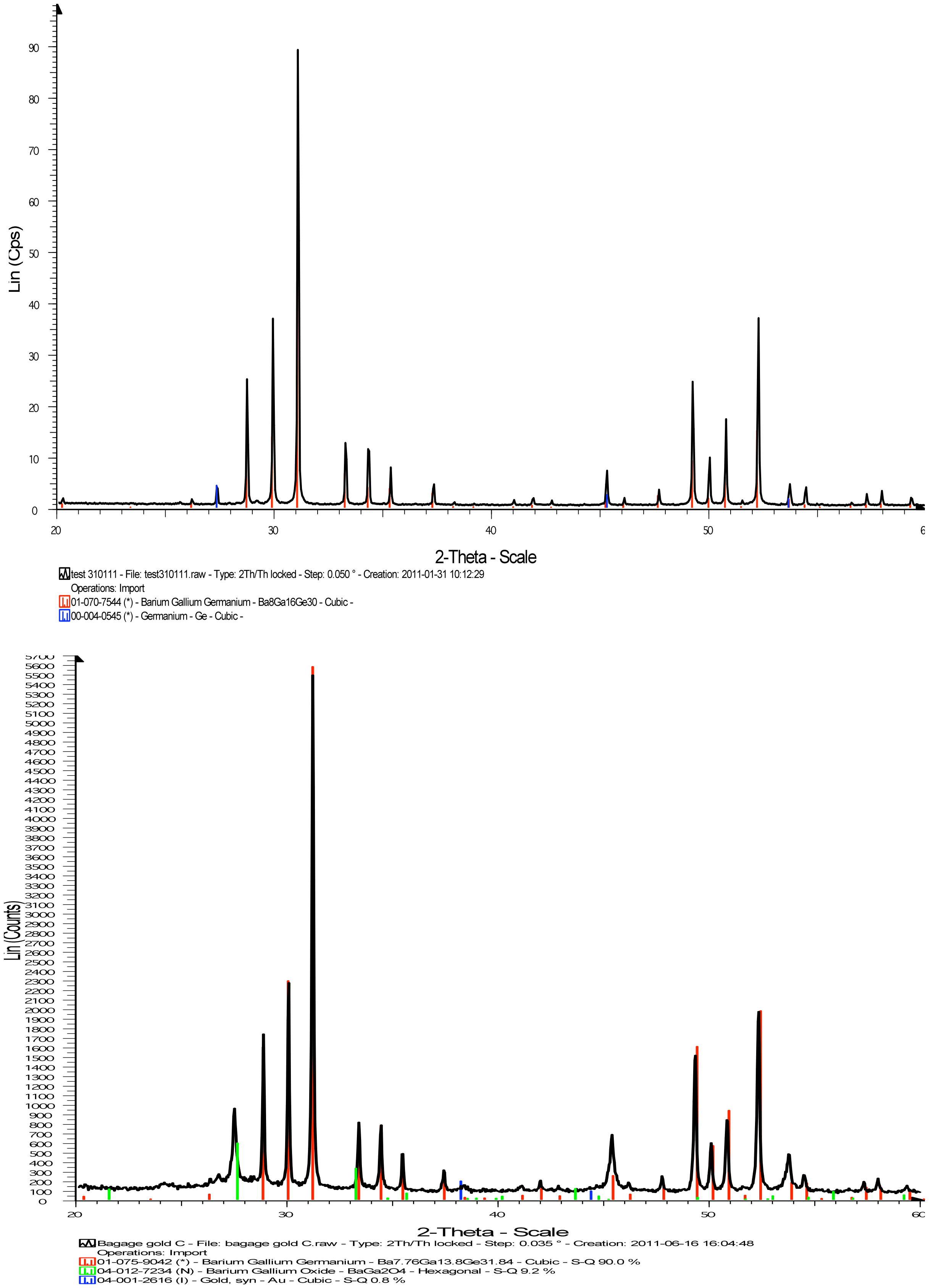

Figure 21. XRD pattern of synthesized clathrate (top) and clathrate with gold nanoinclusion (from tablet sample C) (bottom).

4.2. Gold nanoparticles

The formation of gold seed [16]:

The solution of gold salt and trisodium citrate became pink immediately after adding $NaBH_4$. Thus, $NaBH_4$ is attributed to reduce gold salt in seed solution in this synthesis. At room temperature, trisodium citrate cannot reduce gold salt and it plays a role of capping agent.

The formation of gold nanoparticles in growth solution:

The gold salt in CTAB solution is reduced by ascorbic acid. This is evident by the disappearance of the orange color of the growth solution right after ascorbic acid is mixed with it. Furthermore, the reduction potential of Au^{3+}/Au^{+} is larger than that of ascorbic acid (+0,8 V vs NHE in the presence of Br- and +0,13 V vs NHE, respectively) [16].

However, ascorbic acid is not strong enough to obviously reduce Au^{+} to Au^{0}. Only with the addition of elemental gold nanoparticles (that is, gold seed), the reduction of gold salt by ascorbic acid is achieved.

Right after the formation of Au^{0} nanoparticles, CTAB acts as capping agent that keeps newly formed nanoparticles from aggregation and improves colloidal stability.

4.2.1. UV-Vis spectroscopy

a. Gold solutions after preparation

Figure 22 shows UV-Vis absorption spectra of gold solutions A, B, C and D. Absorption peaks of A, B, C and D are at 523, 524, 526 and 530 nm, respectively. This indicates that particle sizes of gold particles in scaled up solutions are still preserved. To measure the scaled up solutions, they had to be diluted so that the UV-Vis could carry out properly. Only the positions of the peaks were regarded for the estimation of gold particles sizes. The difference between absorbance should not be considered.

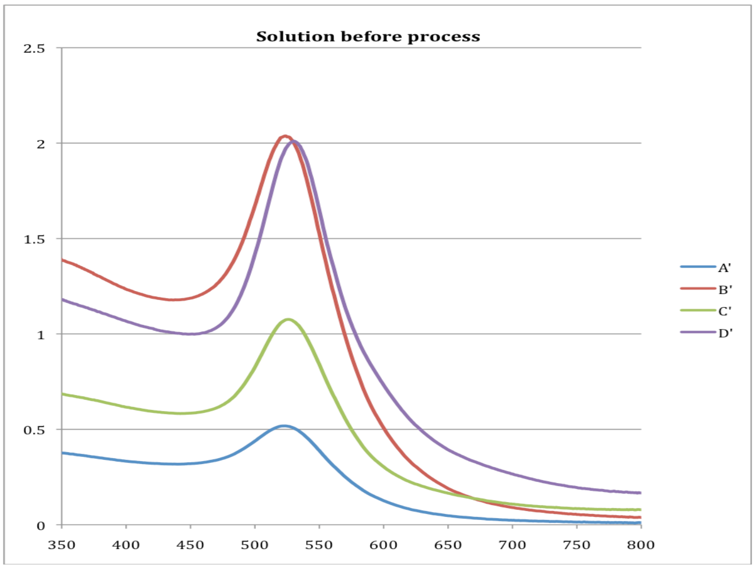

Figure 22. Absorption spectra of solution A, B, C, D after preparation

b. Gold solutions after rotary evaporation

In order to see if the rotary evaporation step facilitates the undesired aggregation of gold particles, UV-Vis spectroscopy was carried out on gold solutions after rotary evaporation and the results are shown in Figure 23. Absorbance of gold solutions peaks in the range of 523-525 nm. This means that gold particle sizes were not severely influenced.

Peak A	Peak B	Peak C	Peak D	Peak M
523 nm	523 nm	525 nm	532 nm	524 nm

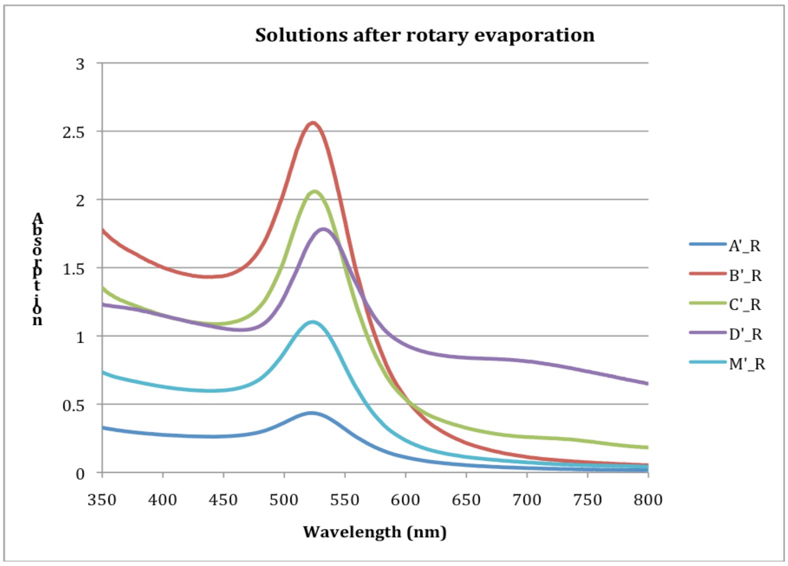

Figure 23. Absorption spectra of A, B, C, D after rotary evaporation

c. Gold solutions after ultracentrifuge

After ultracentrifugation, all peaks of gold solution blue-shifted (Figure 24) compared to that of gold solutions after rotary evaporation.

Peak A	Peak B	Peak C	Peak D	Peak M
520 nm	520 nm	521 nm	528 nm	520 nm

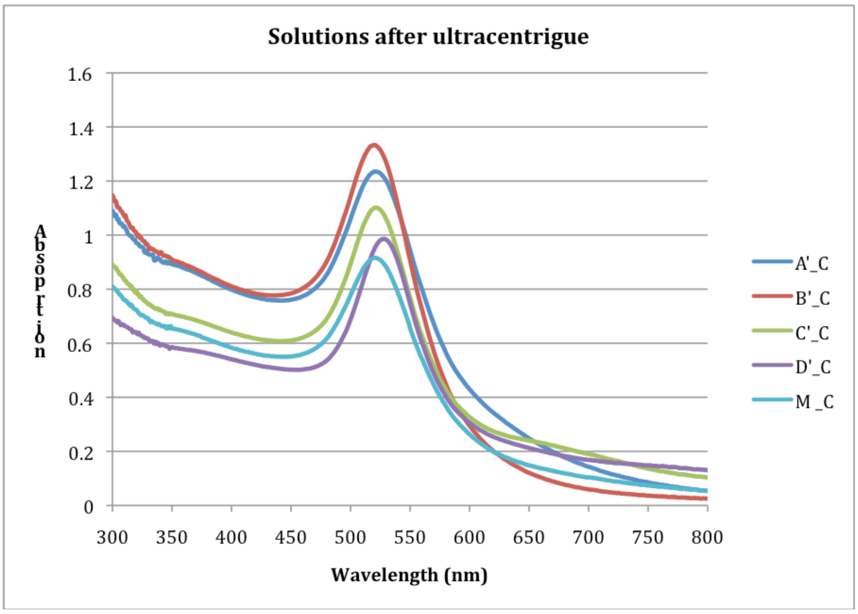

Figure 24. Absorption spectra of A, B, C, D after ultracentrifuge

4.2.2. Dynamic light scattering

a. Gold solutions after preparation

Figure 25 shows the size distribution of the gold solutions prepared in the scaled up syntheses. As explained, the displayed size is not the real size of gold particle but the effective size of a particle containing gold core and surfactant shell. Thus, the displayed size is larger than the expected gold diameter. This fact is shown in the positions of peaks in these DLS results. For samples A, B and C, the fairly sharp peaks at 22,3 nm, 22,7 nm and 35,8 nm, respectively are clearly seen. The standard deviation of these peaks are 9,4%, 11,2% and 8,9%, correspond to solution A, B, and C. The appearance of particles at the range of over 160 nm can be attributed to the existence of dust or big particles. For solution D, the peak is broader, indicating aggregation of the particles. This broad peak is also consistent with the TEM observation of the formation of nanorods in solution D presented in the next section.

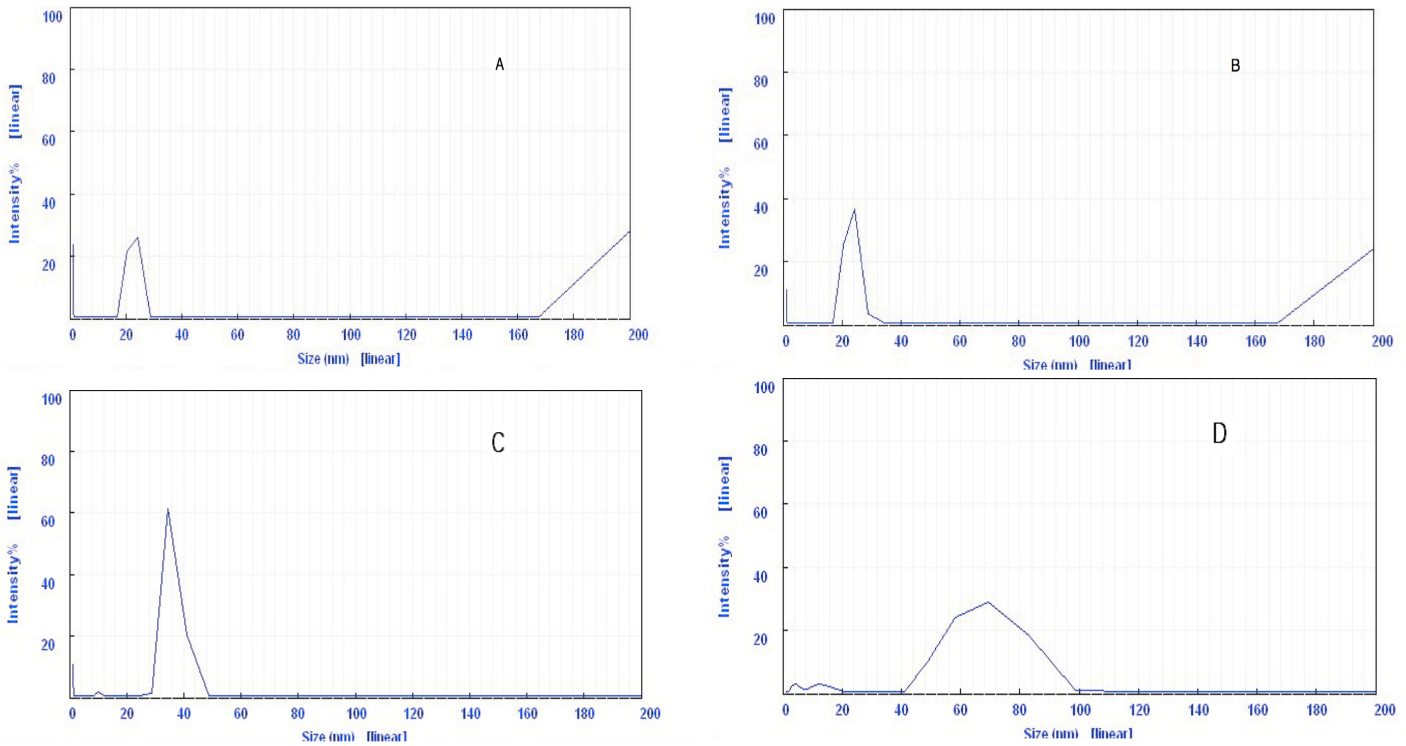

Figure 25. Size distributions of gold solutions A, B, C and D after preparation.

b. Gold solutions after rotary evaporation

Figure 26 shows the size distribution of the gold solutions after rotary evaporation. All peaks are broader, indicating the presence of less well-defined particles after this step. This is reasonable because at this state, in the gold solutions, the gold particles are mixed with high concentration of surfactant, which interferes with the scattered light signal from the gold particles.

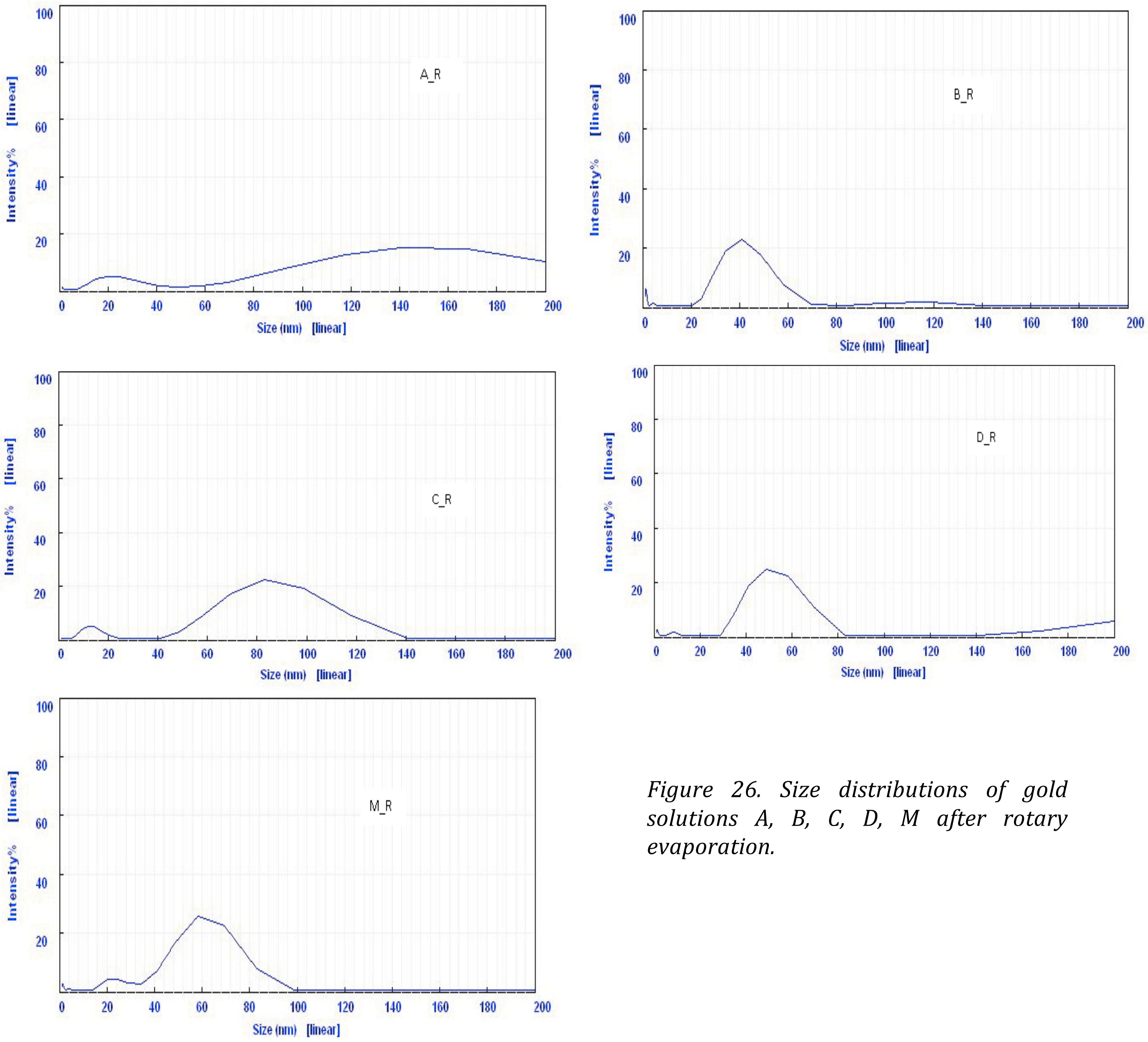

Figure 26. Size distributions of gold solutions A, B, C, D, M after rotary evaporation.

c. Gold solutions after ultracentrifugation

After ultracentrifugation, the size distributions of the gold solutions were again studied. All the peaks of gold solutions become much clearer than that of the solutions after rotary evaporation. This can be attributed to the removal of a significant amount of surfactant after ultracentrifugation that makes the contribution to scattering from the gold particles more distinct under the scope of dynamic light scattering analysis. However, as mentioned before, the displayed particle size is strongly dependent on solvent's properties and particle surface, and the obtained results should not be used as the real particle size of the gold particles. It is also difficult to keep track of the changes in particle sizes after each processing step of gold solution by using DLS.

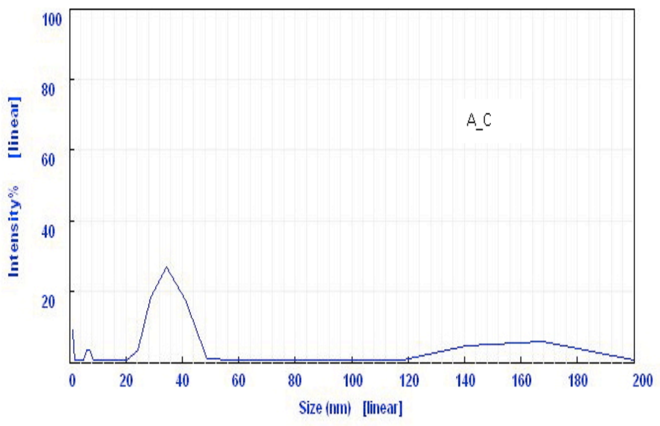

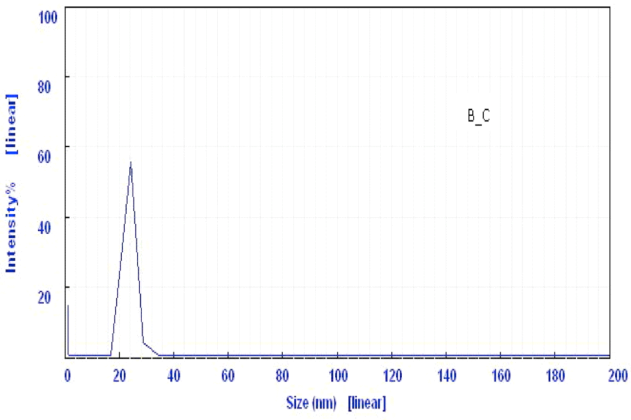

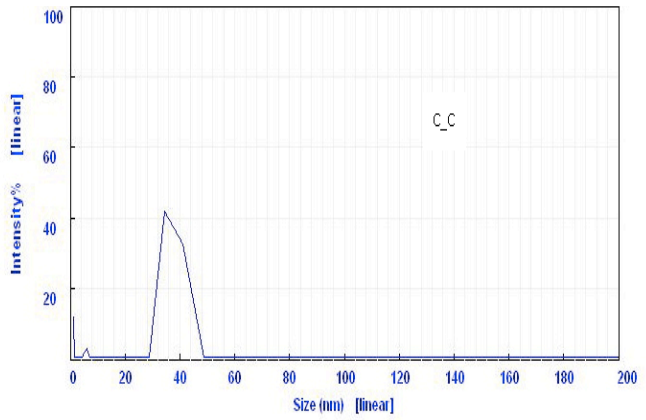

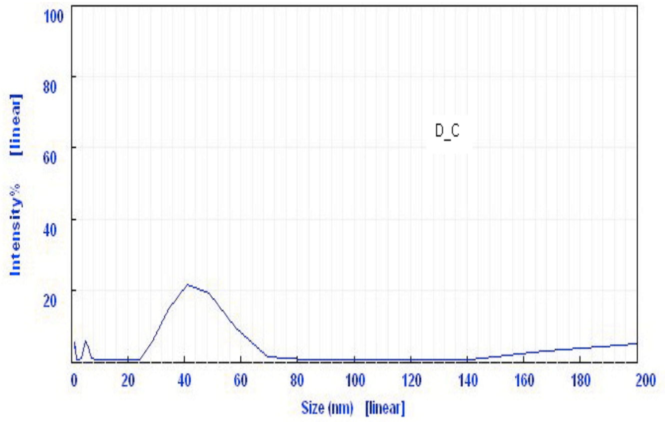

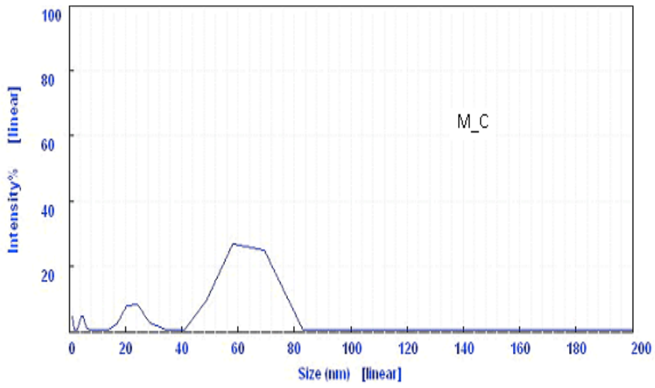

Figure 27. Size distributions of gold solutions A, B, C, D, M after ultracentrifugation.

4.2.3. TEM

From the TEM images (Figure 28), the gold particles are visible. The particle sizes of the gold are as expected from their synthesis: ca. 5, 8, 17, 37 nm for solutions A, B, C and D, respectively. The particle sizes distributions were found to be comparably narrow from the TEM analysis. For sample D, there is a formation of gold particles with non-spherical shape and nanorods, which was also reported in the paper describing the synthesis [16].

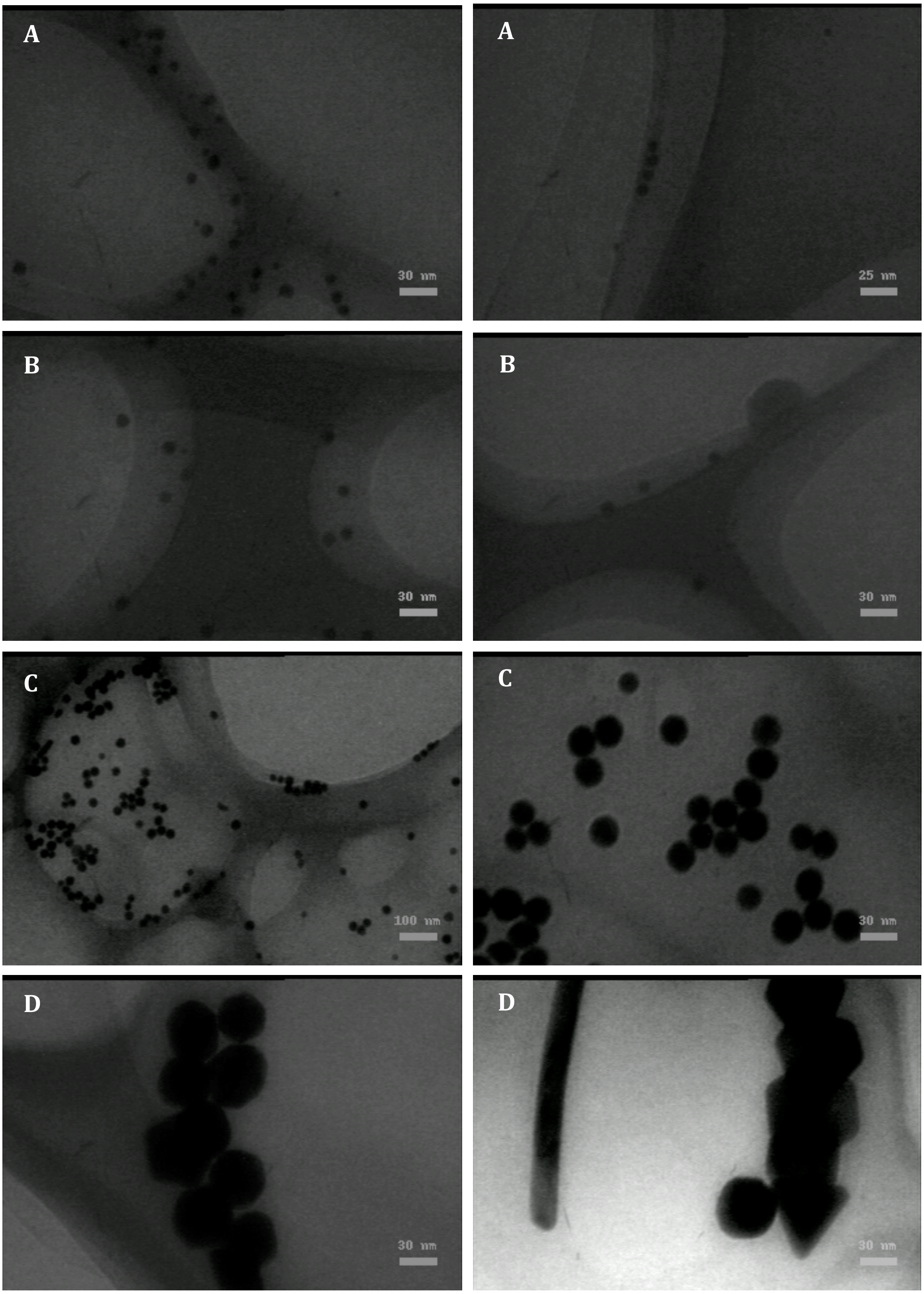

Figure 28. TEM images of gold solutions A, B, C and D.

4.3. Thermogravimetric analysis results

After the freeze-drying, our samples still contained organic impurities in the form of capping CTAB surfactant that needs to be removed. By using TGA, the weight-change of the obtained gold-clathrate powders with temperature can be derived (Figure 29, 30). In Figure 29, the weight change was investigated as the sample was heated to 350°C, then it was kept at that temperature for 4 hours before cooling to room temperature at the rate of 1°C per minute. The mass of the sample was reduced in total 0,5% during this process. From 50°C, the sample's mass decreased. This can be attributed to the desorption of absorbed moisture from the sample.

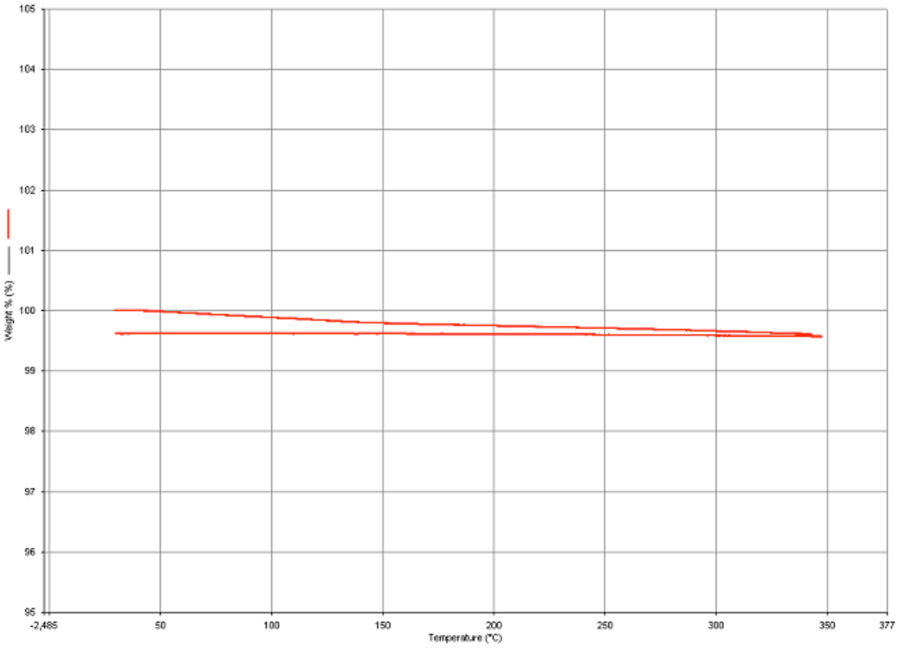

Figure 29. Change of sample's weight with temperature.

Figure 30 shows the weight change with time of the sample during the following heat treatment process: the sample was heated to 350 °C from 30 °C at the rate of 1 °C/min, kept at this point for 4 hours before being heated to 400 °C at 1°C/min. At the 320th minute, corresponding to 350 °C, there was a vertical drop of weight (0,05%). After this decrease, the weight stayed almost the same for about 4 hours before increasing when the temperature was gradually raised to 400 °C. The increment signaled the formation of new substance(s) in the sample as it was heated above 350 °C and can be used to indicate the upper limit of heat treatment temperature. Combining with the unchanged sample mass as it was cooled in Figure 29, it is possible to conclude that CTAB was degraded.

The heat treatment process was chosen based on a previous study [27]. The CTAB degradation effect of the chosen process can also be inferred from results found in other studies [30,31].

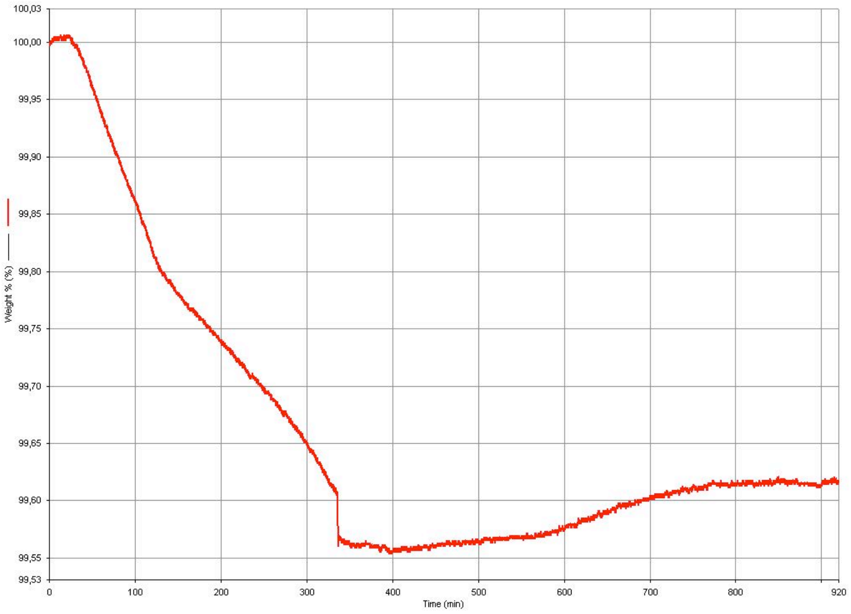

Figure 30. Change of the sample's weight with time

4.4. Thermoelectric performance of obtained samples

In order to evaluate the thermoelectric performance of a material, it is necessary to carry out measurements of thermal conductivity, electrical conductivity and Seebeck coefficient. However, due to limited time, in this work, only the thermal conductivity measurement was performed. Figure 31 shows the changes with temperature of thermoelectric conductivity (κ) of the samples. In figure 28, a relative comparison of κ of all samples at the same temperature is displayed.

From figure 31, it can be seen that when the measurement temperature increases from 22 °C to 600 °C, κ decreases, reaches a minimum in the range of 300 – 500 °C before rising again at 600 °C. The obtained κ values from 350 - 450 ^{o}C should not be taken into account because in this region, the material of the sensor undergoes a phase change affecting its properties and as a consequence, the sensor does not work properly without some compensation, which has not yet been implemented.

To consider the influence of gold nanoparticle size, κ values were plotted as a function of sample (and increasing the gold particle size) at same temperature (Figure 32). The effect of gold nanoinclusions on the thermal conductivity can be seen. It appears that the thermal conductivity of the samples depends on size of gold particles. Except for materials B and M, the thermal conductivity of the other samples is lower than that of the REF sample. It suggests that the thermal conductivity is minimizes at ca. 17 nm size of the nanoinclusions (corresponds to sample C). κ of sample B is significantly higher than that of the other samples. One possible reason for this abnormality is because during measurements, the sensor aged and became unusable, thus a new sensor was used for the measurement of sample B. The measurement technique used is quite sensitive to changes in sensor properties. Thus, the change of sensor may have noticeable influence on the result. The measurement may therefore need to be complemented with additional measurements.

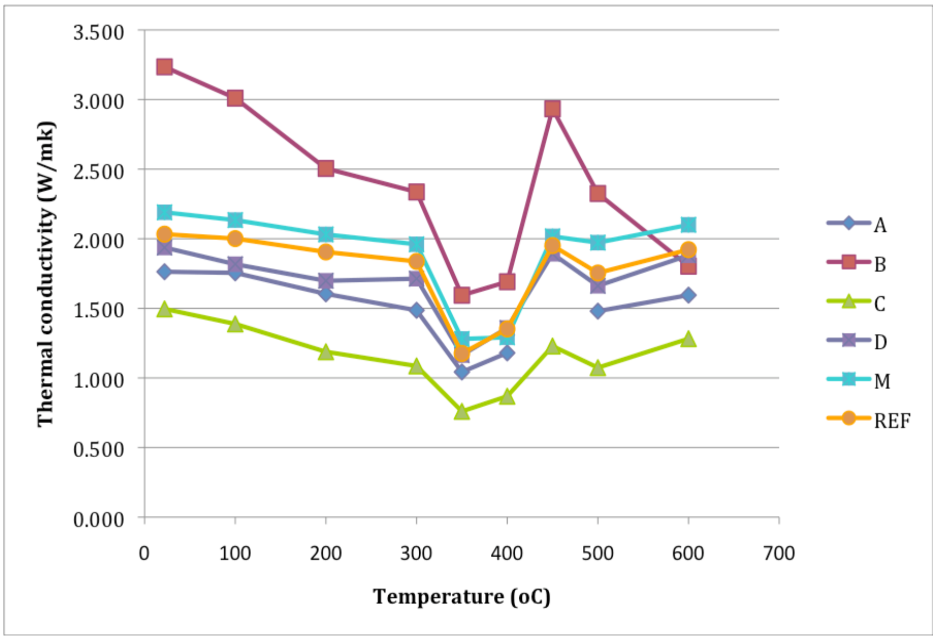

Figure 31. Thermal conductivity changes with temperature of final tablet samples of materials A, B, C, D, M and REF

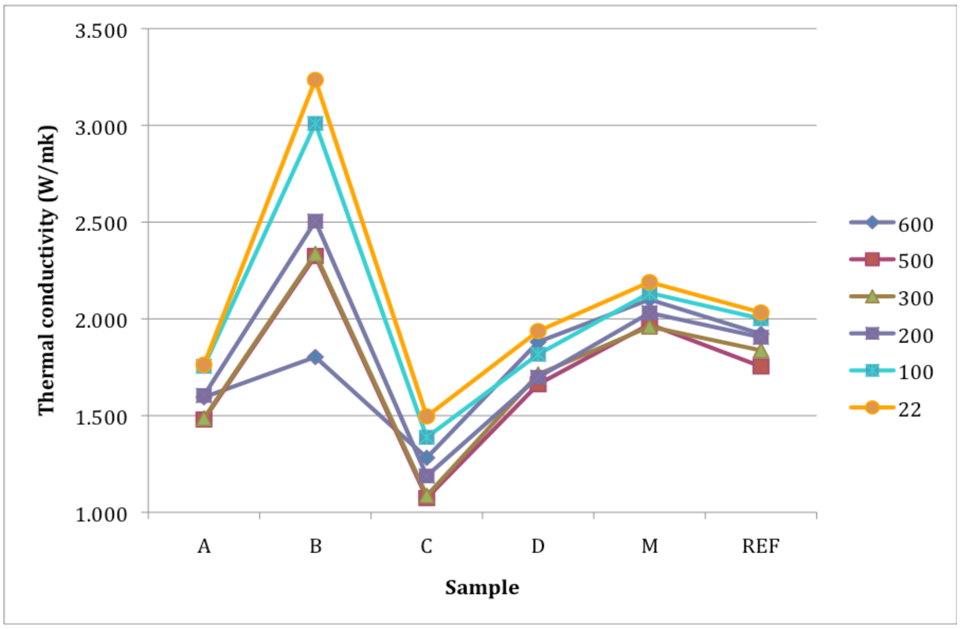

Figure 32. Comparison of samples' thermal conductivity at same temperature.

CONCLUSIONS

In this work:

- Gold nanoparticle suspensions were prepared with different particle sizes: 5, 8, 17, 37 nm and with narrow size distributions. The standard deviations of the obtained solutions were 9,4%, 11,2%, 8,9% for solutions A, B, and C, respectively, according to dynamic light scattering result. For solution D, aggregation of particles and formation of nanorods make it ambiguous to determine its standard deviation.

- The prepared gold particles were introduced into synthesized $Ba_8Ga_{16}Ge_{30}$ clathrate powder. The samples' processing steps indicated that part of the material altered from $Ba_8Ga_{16}Ge_{30}$ to $Ba_{7,76}Ga_{13,8}Ge_{31,84}$ and the formation of barium gallium oxide.

- Thermal conductivity of the final tablet samples was measured. The effect of gold nanoinclusions in reducing thermal conductivity appears in samples A, C, D with narrow size distribution. In this work sample M with large nanoinclusions size range and sample B posses higher thermal conductivity than that of the reference $Ba_8Ga_{16}Ge_{30}$ sample. This point should be confirmed for reliability because the TPS technique is sensitive to changes in measurement conditions. The thermal conductivity was found to be the lowest for the material with the gold particle size of ca. 17 nm, corresponding to sample C.

FUTURE WORK

In order to have more complete understanding of the roles of gold nanoinclusions in thermoelectric germanium clathrate, measurements of electrical conductivity and Seebeck coefficient are needed to identify optimum nanoparticle size in the samples. Also other analyses should be used. The existence of gold nanoparticles in final samples can be studied by field emission scanning electron microscopy, because it can provide pictures of gold nanoparticles in clathrate matrix. Raman scattering and X-ray photoelectron spectroscopy can give information on energy fields around gold nanoinclusions, clarify their role in clathrate, and revealing other substances left in the sample after preparation process. Once issues of finding optimal nanoinclusions size range, its optimal volume ratio, its influence on thermoelectric performance and the removal of impurities are resolved, the competitive applications of gold nanoinclusions in thermoelectric germanium clathrates may be more thoroughly assessed.

BIBLIOGRAPHY

[1]. G. S. Nolas, J. Sharp, H. J. Goldsmid, Thermoelectrics Basic principles and New Materials Development, Springer series in Materials Science, 2001

[2]. G. Jeffrey Snyder and Eric S. Toberer, *Complex thermoelectric materials*, Nature materials, Vol 7, 105 – 112, (2008)

[3]. Suraj J. Thiagarajan, Wei Wang, Ronggui Yang, *Nanocomposites as high efficiency thermoelectric materials*, Annual Review of Nano Research (2008), 441-486

[4]. D. M. Rowe, *Thermoelectrics handbook: Macro to nano,* 2006 by Taylor & Francis Group, LLC

[5]. Joseph R. Sootsman, Duck Young Chung and Mercouri G. Kanatzidis, *New and old concepts in thermoelectric materials*, Angew. Chem. Int. Ed. 2009, 48, 8616-8639

[6]. Simon R. Phillpot, Alan J. H. McGaughey, *Introduction to thermal transport,* Materials today, 2005, 18-20

[7]. D.L. Medlin, G.J. Snyder, *Interfaces in bulk thermoelectric materials: A review for current opinion in colloid and interface science,* Current Opinion in Colloid & Interface Science 14 (2009) 226-235

[8]. Mercouri G. Kanatzidis, et al., *Nanostructured thermoelectrics: Big efficiency gains from small features,* Adv. Mater. 2010, 22, 3970-3980

[9]. Peter Rolg, *Formation of clathrates,* Proceeding of 2005 International Conference on Thermoelectrics, 2005 IEEE, 443-448

[10]. V. L. Kuznetsov, et al., *Preparation and thermoelectric properties of* $A_8^{II}B_{16}^{III}B_{30}^{IV}$ *clathrate compounds*, Journal of Applied Physics, Volume 87, Number 11, 7871-7875, (2000)

[11]. M. Christensen and B. B. Iversen, *Host structure engineering in thermoelectric clathrates,* Chem. Mater. 2001, 19, 4896-4905

[12]. Ali Saramat, et al., Thermal stability and phase purity in polycrystalline $Ba_8Ga_xGe_{46-x}$, Journal of Electronic Materials, DOI: 10.1007/s1164-008-0643-9

[13]. H. Anno, et al., *Thermoelectric properties of* $Ba_8Ga_xGe_{46-x}$ *clathrate compounds*, 21st Proceeding of International Conference on thermoelectrics, 2002, 77-80

[14]. A. Saramat, G. Svensson and A. E. C. Palmqvist, *Large thermoelectric figure of merit at high temperature in Czochralski-grown clathrate* $Ba_8Ga_{16}Ge_{30}$, Journal of Applied Physics 99, 023708 (2006)

[15]. Zhen Xiong, et al., *Effects of nano-TiO_2 dispersion on the thermoelectric properties of filled-skutterudite $Ba_{0.22}Co_4Sb_{12}$*, Solid State Sciences 11 (2009) 1612-1616

[16]. Nikhil R. Jana, et al, *Seeding Growth for Size Control of 5-40 nm diameter Gold nanoparticles,* Langmuir 2001, 17, 6782-6786

[17]. David J. Scott, Stephen E. Harding and Arthur J. Rowe, *Analytical ultracentrifugation: techniques and methods,* Cambridge, UK: RSC Publishing, (2005)

[18]. Daniel Cederkrantz, Thermoelectric $Ba_8Ga_{16}Ge_{30}$ clathrates for waste heat recovery, ISSN: 1652-943X

[19]. Zeki Berk, *Food process engineering and technology,* Elsevier 2009, ISBN: 9780123736604

[20]. C. Suryanarayana, M. Grant Norton, X-ray diffraction: a practical approach, New York: Plenum, cop. 1998

[21]. B. Palpant, et al., *Optical properties of gold clusters in the size range 2 – 4 nm*, Physical review B, Volume 57, number 3, 1998, 1963 - 1970

[22]. A. Kawabata and R. Kubo, *Electronic Properties of Fine Metallic Particles. II. Plasma Resonance Absorption*, Journal of the Physical Society of Japan, 21, (1966), 1765-1772.

[23]. Stephan Link and Mostafa A. El-Sayed, *Spectral properties and relaxation dynamics of surface Plasmon electronic oscillations in gold and silver nanodots and nanorods*, J. Phys. Chem. B 1999, 103, 8410-8426

[24]. Vincenzo Amedola and Moreno Meneghetti, *Size Evaluation of Gold Nanoparticles by UV-vis spectroscopy*, J. Phys. Chem. C 2009, 113, 4277-4285

[25]. *Dynamic Light Scattering: An introduction in 30 minutes*, DLS Technical note, Malvern Instruments, Mark656-01

[26]. P. J. Haines, *Principles of thermal ananlysis and calorimetry,* Royal Society of Chemistry Paperbacks, 2002

[27]. D. Grosso et al., *Highly oriented 3D hexagonal silica thin film produced with cetylmethylammonium bromide,* J. Mater. Chem. 2000, 10, 2085-2089

[28] Silas E. Gustafsson, *Transient plane source techniques for thermal conductivity and thermal diffusivity measurements of solid materials,* Rev. Sci. Instrum. 62 (3), 1991, 797-804

[29]. http://www.hotdiskinstruments.com/products.html

[30]. Hao Tang, et al., *Surfactant-assisted alignment of ZnO nanocrystals to superstructures,* J. Phys. Chem. B 2008, 112, 4016-4021

[31]. Limin Huang, et al., *Synthesis of microporous molecular sieves by surfactant decomposition,* J. Matter. Chem., 2001, 11, 610-615